Persistence and plasticity of bona fide T follicular memory cells

Marco Künzli[1*], David Schreiner[1*], Tamara Pereboom[1], Nivedya Swarnalekha[1], Jonas Lötscher[2], Yusuf I. Ertuna[2], Julien Roux[2], Florian Geier[2], Christoph Hess[2,3], Justin T. Taylor[4], Carolyn G. King[1,2,5**]

[1]Immune Cell Biology Laboratory
[2]Department of Biomedicine, Basel University Hospital and University of Basel, CH-4031 Basel, Switzerland
[3]Department of Medicine, CITIID, University of Cambridge, Cambridge, UK
[4]Vaccine and Infectious Disease Division, Fred Hutchinson Cancer Research Center, Seattle, USA

[5]Lead contact

*Equal first authors

**Correspondence: carolyn.king@unibas.ch

To whom correspondence should be addressed:

Carolyn King
Department of Biomedicine
Basel University Hospital
University of Basel
Hebelstrasse 20
CH-4031 Basel, Switzerland
Email: carolyn.king@unibas.ch
Tel: +41 61 907 15 68 Fax: +41 61 265 34 20

Running title: TFH memory cell persistence, identity and function

SUMMARY

T follicular helper (TFH) cells regulate antibody production. Following infection or vaccination, effector TFH cells give rise to long-lived memory TFH cells. The survival requirements, lineage flexibility and impact of TFH memory cells have not been fully elucidated. In this study we determined that TFH memory cells persist to at least 400 days after infection while T cells with a central memory phenotype are largely absent. Single cell RNA sequencing reveals that TFH memory cells express many genes associated with stemness and self-renewal; reconstruction of a developmental trajectory suggests that TFH memory cells occur earlier in pseudotime, giving rise to other Th cell subsets in a linear fashion. Surprisingly, TFH memory cells concurrently express a distinct metabolic signature similar to trained immune cells, including elevated expression of mTOR, HIF-1 and cAMP regulated genes. TFH memory cell survival is mediated by ICOS signaling which acts as an integrator of glycolytic and self-renewal programming. Inhibition of ICOS at late time points leads to a reduction in TFH memory cells concomitant with decreased splenic plasma cells and circulating antibody titers. These results highlight the metabolic heterogeneity underlying distinct CD4 memory T cell subsets, linking TFH memory cell survival to sustained humoral immunity.

HIGHLIGHTS

- TFH memory cells are long-lived and transcriptionally distinct from T central memory cells
- TFH memory cells are multipotent following recall
- TFH memory cells can be maintained in the absence of but requires ICOS signaling and glycolysis
- TFH memory cells support late phase antibody production by splenic plasma cells

INTRODUCTION

Successful vaccination depends on the generation of protective antibodies that prevent subsequent infection. Antibody development relies on interactions between germinal center B cells and T follicular helper (TFH) cells, a specialized subset of CD4 T cells that provides growth, differentiation and survival signals to developing B cells (Crotty, 2011). TFH cells are generated following vaccination or infection and have been shown to give rise to long lived memory TFH cells (Hale and Ahmed, 2015). Importantly, the number of circulating TFH cells has been shown to correlate with the number of blood plasmablasts following vaccination in humans, and can be boosted to improve long-lived antibody production (Bentebibel et al., 2013; Crotty and Ahmed, 2018; Hill et al., 2019). These data suggest that targeted generation of TFH memory cells may be a rational approach for improving vaccine design. Despite the importance of TFH cells for supporting productive antibody responses, the signals promoting maintenance and survival of the TFH memory cell compartment are not well understood. In many cases, this is complicated by a gradual loss of phenotypic markers

typically associated with TFH cell effectors, including PD1 and CXCR5, as well as decreased stability of the CD4 memory compartment compared to CD8 memory T cells (Hale et al., 2013; Homann et al., 2001; Marshall et al., 2011; Pepper et al., 2011; Williams et al., 2008). In addition, the relationship between T central memory (TCM) cells and TFH effector cells, which share several surface markers and transcription factors including CXCR5, ICOS, Tcf7, STAT3 and Id3, is not clear (Choi et al., 2015; Hale et al., 2013; Ma et al., 2012; Marshall et al., 2015; Siegel et al., 2011; Tian et al., 2017). The development of TCM cells with increased secondary differentiation plasticity and expansion was shown to be dependent on Bcl6, ICOS and B cells, all of which are similarly required for TFH cell differentiation (Pepper et al., 2011). In addition, early TFH effectors share many core features with CD8 TCM cells and demonstrate superior differentiation into long-lived memory cells compared to Th1 effectors (Choi et al., 2013). Recently, a TCM precursor signature, including markers for lymphoid homing (Ccr7) and survival (Bcl2), was identified among antigen-specific effector cells responding to LCMV (Ciucci et al., 2019). This signature, however, was exclusively detected in Th1 and not TFH effector subsets. Although these findings suggest that the precursors of TCM and TFH memory cells are distinct, they do not address whether TCM may derive from TFH effectors or vice versa. Furthermore, whether TFH memory cells maintain the flexibility to differentiate into diverse secondary effectors remains a controversial issue, with evidence both for and against TFH memory cell plasticity (Hale et al., 2013; Keck et al., 2014; Luthje et al., 2012; Pepper et al., 2011).

In this study we determined that TFH memory cells are maintained to at least 400 days after infection, while TCM cells are subject to attrition. Single cell transcriptomic

analysis and epigenetic profiling revealed that TFH memory cells constitutively engage a glycolytic metabolism while maintaining their ability to generate diverse secondary effectors. Sustained ICOS signals are required to preserve mTOR and Tcf7 dependent gene expression in TFH memory cells, with late ICOS blocking leading to a decline in TFH memory cell survival. Strikingly, ICOS blocking also led to a reduction in circulating antibody titers and splenic plasma cells, highlighting an underestimated contribution of TFH memory cells in supporting late phase humoral immune responses.

RESULTS

TFH memory cells are long-lived but susceptible to NAD induced cell death during isolation

TFH cells were recently described to express high levels of the purinergic receptor P2X7 receptor (Iyer et al., 2013; Proietti et al., 2014). P2X7R is an ATP-gated cation channel that can be ADP ribosylated by the cell surface enzyme ARTC2.2, rendering certain cell types, including regulatory T cells (Tregs) and resident memory T cells, susceptible to NICD during isolation from the tissue (Aswad et al., 2005; Fernandez-Ruiz et al., 2016). Injection of an ARTC2.2 blocking nanobody (NICD-protector) prior to organ harvest has been shown to protect these subsets from NICD and improve their recovery from lymphoid organs (Borges da Silva et al., 2019; Hubert et al., 2010). To determine whether inhibition of ARTC2.2 could also improve the recovery of TFH cells at effector and memory time points, we harvested antigen-specific T cells from NICD-protector treated mice at various time points after LCMV infection. Polyclonal LCMV specific CD4+ T cells were enriched using tetramer staining for

Ia^b:$NP_{309-328}$ (NP-specific) or IA^b:GP_{66-77} (GP66-specific) and analyzed for expression of TFH associated surface markers (Hale et al., 2013; Marshall et al., 2011). In untreated mice, TFH effector cells were clearly identified at day 15 after infection, but were largely absent by day 43 (Figures S1A and Figure 1A). In contrast, treatment with NICD-protector resulted in a significant recovery of TFH cells at all time points and with both T cell specificities, indicating a larger expansion and more prolonged survival of TFH cells than previously appreciated (Figure 1A-1C). As the number of GP66-specific TFH cells was approximately 4-fold higher than NP-specific TFH cells, we focused our subsequent analyses on the GP66-specific T cell compartment (Figure S1B). Two-dimensional visualization of the cytometry data by *t*-distributed stochastic neighbor embedding confirmed that NICD-protector preferentially rescued cells with high expression of P2X7R (Figure 1B). NICD-protector also significantly improved the recovery of $PSGL1^{hi}Ly6C^{lo}$ (hereafter $Ly6C^{lo}$ Th1) memory cells but had minimal impact on more terminally differentiated $PSGL1^{hi}Ly6C^{hi}$ (hereafter $Ly6C^{hi}$ Th1) memory cells, consistent with the levels of P2X7R expression on these subsets (Figures 1C, 1E, and S1C). After day >400, TFH memory cells were maintained in LCMV infected mice although the mean cell fluorescence of PD1 on this population was decreased compared to earlier time points (Figures 1A and 1C). In contrast, $Ly6C^{lo}$ Th1 memory cells, previously shown to contain a substantial proportion of TCM cells, were 10-fold decreased compared to TFH and $Ly6C^{hi}$ Th1 memory cells, suggesting either a survival defect or conversion into one of the remaining memory cell subsets (Figures 1A and S1C). TFH cells isolated at late time points after infection were further phenotyped by flow cytometry and characterized by high expression of FR4, CD73, CXCR4, ICOS and Bcl6

compared to Ly6C^{hi} and Ly6C^{lo} Th1 memory cells (Figures 1D and 1E). Although a similar phenotype was observed on polyclonal NP-specific TFH cells isolated from LCMV infected mice (Figure S1A), monoclonal T cells from SMARTA or NIP T cell receptor (TCR) transgenic strains specific for LCMV GP66:I-A^{b} and NP309:IA^{b} respectively, generated significantly fewer numbers of TFH memory cells after LCMV infection (Figure S1D) (Nance et al., 2015; Oxenius et al., 1998). These observations are consistent with previous reports showing a gradual decline of TFH associated markers on transferred monoclonal populations as well as the tendency of different types of TCR transgenic T cells to undergo distinct and more limited patterns of differentiation (Hale et al., 2013; Marshall et al., 2011; Tubo et al., 2013).

TFH memory cells are transcriptionally distinct from TCM

To gain further insight into CD4 memory T cell heterogeneity and regulation we performed single-cell RNA sequencing (scRNA-seq) on GP66-specific T cells isolated at day >35 post-infection. Principal component analysis (PCA) based on genes with the highest biological variance was used to provide a low dimensional representation of the data and as a basis for hierarchical clustering of the cells (Figure 2A and S2B). We examined 7 distinct memory populations that were enriched for genes associated with TFH cells (clusters 1-3, 37% of cells), TCM (clusters 4 and 5, 45% of cells) and Th1 memory cells (clusters 6 and 7, 18% of cells) (Figures 2A, 2B and S2B). The top defining genes in the TFH clusters included established TFH markers such as *Izumo1r* (encoding FR4), *Pdcd1, Sh2d1a*, as well as transcription factors known to be expressed by CD4 memory cells, including cells *Klf6, Jun and Junb* (Figures 2B and 2C) (Crawford

et al., 2014). TCM and Th1 clusters (4-7) exhibited higher expression of *IL-7r, S100a4, S100a6, Selplg* and various integrins (Figures 2B and 2D), while clusters 6 and 7 were enriched for genes strongly associated with Th1 differentiation including *Cxcr6, Ccl5, Nkg7* and *Id2* (Figures 2B and 2E). Among Th1 clusters, cluster 7 represented the subset highest in *Selplg*, *Ly6c2* and *Il7r*, while cluster 6 expressed higher levels of *Cxcr6* and *Id2* and exhibited signatures of dysfunction and exhaustion (Figures S2D-S2F) (Ciucci et al., 2019; Martinez et al., 2015). Cluster cell-type identities were further confirmed by scoring each cell for signature genes obtained from publicly available datasets and examining the distributions of these scores across clusters (Figures 2F and S2C). TFH and Th1 signatures matched well with clusters 1-3 and 6-7 respectively, while clusters 4, 5 and 7 were enriched for the TCM precursor signature reported by Ciucci et. al. (Figure 2F) (Ciucci et al., 2019). Clusters 4 and 5 had the highest *Ccr7* transcription, which negatively correlated with *Cxcr5* across all cells (Figure 2G). To facilitate visualization of the relationship between *Ccr7* and *Cxcr5*, we plotted expression levels imputed using the Seurat R package (Figure 2H) (Satija et al., 2015). Within TFH clusters 1-3, we observed a gradient in *Cxcr5* and *Pdcd1* expression while *Izumo1r* remained stable, serving as a much cleaner transcriptional marker of the boundary between TFH memory and TCM cells (Figures 2G and 2I). We found a similar negative correlation between protein expression for CCR7 and CXCR5, the highest CCR7 expressing cells falling within the Ly6C^{lo} Th1 compartment (Figures 2J, S2H). The use of FR4 as a marker for TFH identity improves upon existing strategies, which either allocate too many TFH cells into a TCM gate or depend upon markers like PD1 and CXCR5 which are known to decline over time. In addition, TFH memory cells

expressed a partially overlapping transcriptional signature with tissue resident memory cells, highlighting the non-circulating status of this population (Figure S2G). Notably, *Hif1a*, a transcription factor normally associated with glycolysis, was one of the top genes expressed by TFH memory cells, consistent with the recently reported high expression of this transcription factor in TFH effectors and resident memory cells (Figure 2B) (Cho et al., 2019; Hombrink et al., 2016; Zhu et al., 2019).

TFH memory cells are constitutively glycolytic

In addition to *Hif1a* expression, TFH memory cells were enriched for mTOR and cAMP regulated genes suggesting a metabolic signature similar to that observed in trained immune cells (Figures 3A, S3A and S3B) (Bekkering et al., 2018; Cheng et al., 2014; Saeed et al., 2014). Enhanced activation of mTOR regulated genes was also observed following secondary analysis of microarray data on bulk sorted Smarta TFH memory cells as well as recently published single cell data from GP66-specific TFH memory cells (Figures S3C and S3D), and was further confirmed by qpcr of selected Raptor regulated genes in sorted CD4 GP66-specific memory T cell populations (Figure 3B) (Zeng et al., 2016). These data indicated that TFH memory cells may constitutively engage a glycolytic metabolism. To assess mTORC1 activity, we measured phosphorylation of TORC1-target ribosomal protein S6 (p-S6) directly after T cell isolation (Figures 3C and S3E). Both GP66-specific TFH cells as well as CD44+ TFH cells, which have phenotypic characteristics similar to antigen-specific TFH cells (Figure S3F), exhibited increased p-S6 compared to Th1 memory cells (Figure 3C, Figure S3E). Consistent with mTOR activation, TFH memory cells had increased uptake of the

fluorescent glucose analog 2-NBDG, and an increased baseline extracellular acidification rate (ECAR) (Figure 3D and 3E). Alongside this apparent increase in glycolytic metabolism, TFH memory cells had slightly decreased expression of the amino acid transporter CD98 and the transcription factor c-myc compared to Th1 memory cells, indicating that not all measures of anabolic activity are increased in these cells (Figure S3G and S3H). In addition, the shift toward glycolysis observed in TFH memory cells was accompanied by a slight reduction in baseline oxygen consumption rate (OCR) compared to Th1 memory cells, whereas the maximum respiration, and spare respiratory capacity was similar between these two populations (Figure S3I). At the transcriptome level, TFH memory cells appeared to be enriched for genes associated with oxidative phosphorylation and mitochondrial respiration a signature commonly associated with CD8 memory T cell survival (Figure S3J). As TFH effectors were previously reported to have decreased mTOR activation and reduced glycolysis (Yang et al., 2016; Zeng et al., 2016), we also assessed the metabolic capacity of these cells isolated at day 10 after infection, reasoning that NICD-protector might improve their survival and fitness. At this time point, TFH effectors had slightly reduced basal ECAR compared to Th1 effectors but demonstrated normal glycolytic flux following the addition of FCCP (Figure S3K). In addition, and similar to TFH memory cells, TFH effectors had equivalent baseline and maximal respiratory capacity as Th1 effectors indicating that NICD-protector preserves the metabolic fitness of TFH cells after isolation at both early and late time points after infection (Figure S3L). To assess whether constitutive glycolysis/mTOR signaling are required to maintain long lived TFH cells, we next examined TFH cell survival in mice treated with the glycolysis inhibitor 2-

deoxyglucose (2-DG) and rapamycin starting at day >40 after LCMV infection. After two weeks of 2-DG/rapamycin treatment, both the percentage and number of TFH memory cells were significantly decreased, with the remaining TFH memory cells showing a reduction in size consistent with reduced mTOR activation (Figures 3F, 3G and S3M) (Ray et al., 2015). Signaling through P2X7R was recently suggested to restrain mTOR activation, leading to improved survival of CD8 memory T cells (Borges da Silva et al., 2019). In contrast, P2X7R signals have been shown to restrain accumulation of TFH effector cells in Peyer's Patches (Proietti et al., 2014). To assess whether P2X7R signals promote or restrain TFH memory cell survival, we generated radiation bone marrow chimeras with a mixture of wild-type and P2X7R-/- bone marrow. Sixty days after LCMV infection, P2X7R-/- T cells generated an increased proportion of all memory cells, with the most significant increase in the TFH memory compartment (Figure 3H, 3I). These data demonstrate that P2X7R is a key negative regulator of TFH memory cell accumulation and are consistent with a role for P2X7R in restraining mTOR activation.

TFH memory cells can survive in the absence of antigen

Glycolytic metabolism in T cells is often associated with activation and effector cell proliferation. To assess whether TFH memory cells are responding to ongoing antigen stimulation we assessed Nur77 expression within the TFH memory compartment of LCMV infected Nur77 reporter mice. Approximately 30% of PSGL1^{lo}Ly6C^{lo} TFH cells were Nur77 positive, with a slightly higher percentage in the CXCR5^{hi}PD1^{hi} TFH compartment (Figure 4A). Although PD1 expression was

moderately increased on Nur77+ compared to Nur77- TFH memory cells, it was much higher on both of these populations compared to non-TFH memory cells (Figure 4B). Although these data indicate that a fraction of the TFH memory compartment continues to respond to antigen, there was no positive correlation between PD1 expression and 2-NBDG uptake, indicating that glucose uptake within the TFH compartment is unlikely to be related to antigen stimulation (Figure S4A). Consistent with this idea, increased 2-NBDG uptake was maintained by TFH memory cells at >400 days of infection, a time point where PD1 expression by TFH memory cells is decreased compared to earlier time points (Figure S4B). To understand whether the glycolytic metabolism observed in TFH memory cells is related to proliferation, we administered bromo-2-deoxyuridine (BrdU) in the drinking water of LCMV infected mice, starting 40 days after infection. After 12-14 days, approximately 4% of PSGL1^{lo}Ly6C^{lo} TFH memory cells incorporated BrdU with a slightly higher proportion CXCR5^{hi}PD1^{hi} TFH cells staining positive for BrdU (Figure 4C). Ly6C^{lo} Th1 memory cells showed a similar level of in vivo cycling with approximately 5% of cells staining for BrdU, while 15% of Ly6C^{hi} Th1 memory cells were BrdU positive, demonstrating more extensive proliferation by this subset (Figure 4C). These data show that the glycolytic phenotype observed in TFH memory cells is not strictly correlated with extensive cell division, although the slightly increased BrdU incorporation by CXCR5^{hi}PD1^{hi} TFH memory cells may be related to ongoing antigen stimulation. To better understand the contribution of antigen to maintaining the TFH memory compartment, we transferred LCMV-specific effector cells isolated at day 10 after LCMV infection into either LCMV infection matched or naive recipients followed by analysis of donor T cell phenotype. Thirty days after primary

infection, Ly6C^{hi} Th1 memory cells were nearly absent in both transfer scenarios, indicating that Th1 effector cells may be susceptible to death at the time point of isolation and transfer (Figure 4D). In contrast, GP66-specfic TFH memory cells were detected in both antigen free (naïve) and infection matched mice, although fewer TFH memory cells were recovered from naïve mice, possibly due to continued expansion of TFH effector cells in LCMV infected recipients between days 10-15 after transfer (Figures 4D, 4E and Figure 1C). In addition, although TFH memory cells isolated from antigen free mice had decreased expression of CXCR5 and PD1, they were clearly identified by high expression of FR4, consistent with scRNA-seq data pinpointing FR4 as a more reliable marker bona fide TFH memory cells (Figures 4D, 4E, 2C, and 2I). Taken together these data underscore the ability of TFH memory cells to survive in the absence of antigen.

TFH memory cells give rise to multiple cell fates upon recall

Despite maintaining a glycolytic phenotype, TFH memory cells are also enriched for genes regulated by Tcf7 and highly express CD27, a marker associated with memory T cell survival, cytokine production potential and stemness, as shown by scRNA-seq (Figures 5A and S5A) (Hendriks et al., 2000; Karmaus et al., 2019; Pepper et al., 2010). Although higher expression of Tcf7 in TFH memory cells translated into higher expression of TCF1 protein, CD27 protein expression was significantly lower in TFH compared to Th1 memory cells (Figures 5B and S5B). To determine if the discrepancy between the CD27 gene expression and protein expression was a result of P2X7R mediated shedding we examined CD27 on memory cells isolated from LCMV

infected mixed bone marrow chimeras reconstituted with an equal mixture of P2X7R-deficient and wild type bone marrow cells (Moon et al., 2006). Here we observed higher expression of CD27 on P2X7R-deficient TFH memory cells compared to both wild type TFH and Th1 memory cells (Figure S5B). Consistent with high expression of both Tcf7 and CD27, TFH memory cells were also enriched for “early memory” associated genes (Figure S5C). In addition, reconstruction of a developmental trajectory using Monocle2 indicated that TFH and Th1 memory cells occupied opposite ends of the pseudotime trajectory, predicting enhanced differentiation plasticity in one of these subsets (Figure S5D and S5E) (Trapnell et al., 2014). To test this in vivo, TFH (FR4^{hi}PSGL1^{lo}Ly6^{lo}) and Th1 (FR4^{lo}PSGL1^{lo}Ly6^{hi} and FR4^{lo}PSGL1^{hi}Ly6^{hi}) memory cells were sorted from LCMV infected mice and transferred into naïve congenic recipients, followed by secondary challenge with LCMV (Figure 5D). Twelve days after recall infection, transferred TFH memory cells differentiated into both TFH and Th1 effectors demonstrating lineage flexibility within this subset (Figures 5E and 5F). In contrast, Ly6C^{lo} Th1 memory cells maintained the capacity to differentiate into both Ly6C^{hi} and Ly6C^{lo} effectors, but gave rise to very few TFH effectors, suggesting more limited plasticity of this subset (Figures 5E and 5F). Consistent with several previous reports, Ly6C^{hi} Th1 memory cells almost exclusively gave rise to Ly6C^{hi} secondary effectors, indicating more terminal differentiation of this subset (Figures 5E and 5F) (Hale et al., 2013; Pepper et al., 2011). Taken together, these data demonstrate that despite engaging an anabolic metabolism often associated with effector cell proliferation and differentiation, TFH memory cells maintain the capacity to differentiate into multiple types of effectors following secondary challenge.

Epigenetic regulation of TFH memory T cells

To assess whether the distinct transcriptional signatures observed in TFH and Th1 memory cells are also apparent at the epigenetic level we compared chromatin accessibility of naïve, Th1 and TFH memory T cells by ATAC-seq (Buenrostro et al., 2013). The majority of called peaks were shared among these 3 populations, with the highest number of unique peaks present in undifferentiated naive CD4 T cells (Figures S6A). Principal component analysis (PCA) revealed that TFH and Th1 memory cells are set apart from naïve T cells along PC1, yet also possessed distinct accessibility profiles from each other along PC2 (Figure 6A). Although no striking differences were observed in the number of differentially accessible chromatin regions annotated to exons, introns or distal intergenic regions between TFH and Th1 memory cells, TFH memory cells had twice the number of differentially open promoter regions (Figures S6B). We therefore compared promoter regions with a high-fold change ($\log_2$ (fold change) > 1 and false discovery rate (FDR) < 0.05) between at least two of the T cell subsets (Figure 6B, S6H). Hierarchical clustering of high-fold change regions resulted in six clusters of genes with common accessibility patterns: e.g. up in naïve, up in memory, up in naïve and TFH memory. For example, the Foxp1 promoter was exclusively accessible in naïve CD4 T cells, consistent with its role as a gate keeper of the naïve to memory T cell transition (Durek et al., 2016). Integrative analysis of ATAC-seq and *in silico* bulk RNA-seq data (derived from scRNA-seq data) revealed a coordination between the promoter accessibility and transcription of genes defining TFH and Th1 memory cell subsets (Figures S6C) (Hale et al., 2013). Consistent with a study that assessed the DNA methylation status of various cytokine loci in TFH and Th1

memory cells (Hale et al., 2013), we observed that the *Gzmb* promoter was exclusively accessible in Th1 memory cells, while the *Ifng* promoter was accessible in both populations, albeit at slightly lower levels in TFH memory cells (Figures S6D). In contrast to this earlier study, however, the promoter accessibility of the hallmark TFH cytokine, IL-21, was restricted to TFH memory cells (Figure S6D). In addition, one of the most accessible cytokine promoter regions in TFH memory cells was the epidermal growth factor-like ligand amphiregulin (*Areg*), notable for its role in restoring tissue integrity after infection (Zaiss et al., 2015). To further assess differences in the transcriptional regulation of TFH and Th1 memory cells, we analyzed enriched binding motifs in called peaks using Hypergeometric Optimization of Motif Enrichment (HOMER) (Heinz et al., 2010). In agreement with the RNA-seq data, TFH memory cells were enriched for motifs belonging to the Tcf7 transcription factor family as well as AP-1 family members which are known to be similarly regulated in CD8 memory cells (Figure 6C) (Lau et al., 2018; Moskowitz et al., 2017). In contrast, Th1 memory peaks exhibited increased Runx and T-box transcription family member binding sites, consistent with the cooperation of these transcription factors in regulating IFNγ and stabilizing Th1 fate by CD4 T cells (Figure S6E) (Djuretic et al., 2007; Kohu et al., 2009). These observations were further validated by applying the single-cell regulatory network interference and clustering (SCENIC) algorithm to scRNA-seq data, which highlighted Tcf7/AP-1 and Runx family members as regulators in TFH memory and Th1 memory, respectively (Figure S6F). We next assessed specific functional pathways in the ATAC-seq data by running gene set enrichment analysis (GSEA) on differentially accessible promoter regions in TFH compared to Th1 memory cells (Figure 6D). Here we observed

increased accessibility in *Rptor* and *Tcf7* regulated genes in TFH memory cells, suggesting that the anabolic and stem signatures of this population are strongly regulated at the epigenetic level (Figure 6D). Finally, using Ingenuity Pathway Analysis (IPA) (Qiagen, version 01-14) to probe the functional regulation of TFH memory cells, we identified ICOS-ICOSL signaling as one of the top pathways enriched in both ATAC-seq and scRNA-seq data sets (Figure 6E) (Kramer et al., 2014). These data raise the possibility that ICOS mediated signals contribute to the maintenance and identity of TFH memory via specific epigenetic modifications.

ICOS signaling maintains TFH memory cell identity and contributes to late phase humoral immune responses

Although ICOS has an established role in primary TFH responses, it's role in maintaining CD4 memory is less clear. ICOS signaling has been shown to induce the expression of Tcf7 in Th17 memory cells that maintain the plasticity to differentiate following stimulation (Majchrzak et al., 2017). ICOS can also induce mTORC1 activation in both TFH effector and T follicular regulatory (TFR) effector cells, leading to further stabilization of the follicular T cell program (Xu et al., 2017; Yang et al., 2016; Zeng et al., 2016). To test the hypothesis that ICOS signals contribute to the integration of stemness and anabolic metabolism in TFH memory cells we treated LCMV infected mice with anti-ICOSL starting at day >50 after infection (Figure 7A). After 12 days of treatment, the number of GP66-specific TFH cells was decreased in anti-ICOSL treated mice (Figures 7B). The TFH memory cells remaining after ICOS blockade had decreased expression of TCF1 as well as reduced activation of mTOR as measured by

cell size (Figure S7A and S7B). To further characterize the effects of anti-ICOSL blocking on TFH memory cells, we performed RNA-seq at day 60 post infection on control and treated mice. Cells from mice treated with anti-ICOSL for 12 days prior to harvest exhibited lower transcription of key TFH genes such as *Pdcd1*, *Cxcr5* and *Bcl6*, while known Th1 survival factors such as *Bcl2* and *Il7r* were increased (Figure 7C). Gene set enrichment analysis showed decline of TFH-defining, resident memory, *Rptor*-regulated and stem cell-associated sets in treated samples compared to controls (Figure 7D). These data demonstrate the importance of ICOS signals in maintaining TFH memory cell identity.

During primary immune responses, ICOS signals promote TFH effector cell localization in B cell follicles and primary germinal center responses (Shi et al., 2018; Weber et al., 2015). To assess whether late ICOS blockade and subsequent decline of the TFH memory cell compartment impacts late phase humoral responses, we measured LCMV-specific antibody titers in the serum at day >60. Here we observed an almost 2-fold decrease in NP-specific antibody titers (Figure 7E). At this late time point after infection, circulating virus-specific antibodies are maintained by plasma cells, approximately 80% of which are localized in the bone marrow compartment (Slifka and Ahmed, 1996; Slifka et al., 1995). However, plasma cells are also observed in the spleen, with an estimated half-life of 172 days (Slifka et al., 1998) (Ndungu et al., 2009). To determine if the decline in antibody titers correlated with fewer plasma cells in the bone marrow or splenic compartments, we measured the number of NP-specific plasma cells by ELISPOT. Here we observed that anti-ICOSL treatment correlated with a two-fold decrease in the number of splenic plasma cells, with no apparent impact on the

number of bone marrow plasma cells (Figure 7E). Assuming that ICOS blocking is 100% efficient and that circulating IgG has a half-life of approximately 8 days, these data reveal a significant and ongoing contribution of splenic plasma cells to antibody maintenance at this time point (Figure S7C). To further assess humoral immune responses, we assessed virus specific B cell responses using an NP-tetramer in combination with a decoy reagent to exclude non-specific B cells (Taylor et al., 2012). Neither the total number of NP-specific memory B cells nor the number of IgD, IgM or swIg memory B cells were affected by ICOS blockade (Figure S7D). There was a significant decrease, however, in the number and proportion of GL7+ B cells (Figure S7E). Of note, these cells did not express Fas, a marker normally associated with GC B cells and that when absent, has been reported to preferentially support plasma cell differentiation (Figure S7E) (Butt et al., 2015). Taken together, these data demonstrate an essential role for ICOS signaling in maintaining the TFH memory compartment and plasma cell survival in the spleen.

DISCUSSION

In this study we determined that TFH memory cells are surprisingly long-lived and maintain differentiation plasticity following challenge infection. TFH memory cells can survive in the absence of antigen, but require ICOS signaling to sustain both mTOR and Tcf7 dependent gene expression, both of which are critical for TFH memory cell identity. In addition, we determined that TFH memory cells actively support late phase antibody production by splenic plasma cells, thereby contributing to the maintenance of circulating antibody titers.

Earlier studies reported that TFH memory cells have a 'rested down' phenotype, with decreased or absent expression of CXCR5 and PD1, respectively (Hale et al., 2013; Marshall et al., 2011). Here we determined that short term treatment with NICD-protector significantly improved the recovery of TFH memory cells, preserving their expression of TFH defining surface markers including PD1, CXCR5 and FR4 (Figure 1). Interestingly, while TFH memory cells are detected as late as day 400 after infection, Ly6C^{lo} Th1 memory cells that are enriched for TCM associated genes are largely absent (Figure 1A and 2F) (Ciucci et al., 2019) (Marshall et al., 2011).

Two recent studies reported that the differentiation of TFH effectors requires mTOR signaling and glycolysis (Yang et al., 2016; Zeng et al., 2016). Our scRNA-seq and functional data demonstrate that this metabolic phenotype is sustained in TFH memory cells, well after viral clearance and resolution of the immune response (Figures 3D, 3F, and S3M). Activation of mTOR does not strictly require antigen, although sustained antigen availability improves the recovery of TFH memory cells with increased expression of PD1 (Figures 4A and 4D). Accordingly, mTOR dependent gene expression is also observed in Smarta TFH memory cells isolated at day 150 after infection when PD1 expression is not detected (Figure S3C) (Hale et al., 2013). Moreover, polyclonal GP66-specific TFH memory cells isolated at day 412 after infection, a time point where antigen is unlikely to be present, maintain high levels of 2-NBDG uptake (Figure S4B).

Our data additionally demonstrate that mTOR gene regulation is maintained concurrently with Tcf7 dependent gene expression (Figures 3A, S3A, 5A, 6C, and

6D). In general, effector T cell differentiation is associated with a more glycolytic metabolism while memory T cells have a shift toward oxidative metabolism (Bantug et al., 2018). Previous studies have shown that inhibition of mTOR signals can promote the generation of both CD4 and CD8 memory T cells; mTOR activation was also recently shown to mediate the differentiation of metabolically quiescent Tcf7 positive Th17 cells into inflammatory Th1 effectors (Araki et al., 2009; Karmaus et al., 2019; Pearce et al., 2009; Ye et al., 2017). On the other hand, CD4 memory T cells require Notch dependent glucose uptake for survival, and CD8 T cells with enforced glycolytic metabolism are able to generate memory T cells with robust recall capacity, albeit with a bias toward the CD62L^{lo} T effector memory (TEM) phenotype (Maekawa et al., 2015; Phan et al., 2016). In line with these findings, human CD4 TEM cells have an increased glycolytic reserve and depend on glycolysis to maintain mitochondrial membrane potential, regulating both survival and recall potential (Dimeloe et al., 2016). These latter findings suggest that while engagement of a specific metabolic pathway may not universally drive the differentiation of memory T cells, different types of memory T cells may preferentially engage metabolic pathways that are tuned to a particular immune context (e.g. availability of cytokines, nutrients, antigen, etc.).

Our data further implicate ICOS in sustaining mTOR and stemness features in TFH cells (Figures 7A-D, and S7A). These observations suggest that maintenance of TFH memory phenotype is an active process, and that in the absence of ICOS signaling, TFH memory cells may re-localize and acquire Th1 memory cell characteristics (Weber et al., 2015). This idea is consistent with experiments demonstrating the inherent plasticity of TFH memory cells (Figures 5E and 5F), although under unperturbed

conditions, ICOS mediated retention of TFH memory cells in proximity to B cells may stabilize their identity and secondary effector potential. ICOS signals have previously been shown to be required for the maintenance of CD4 TEM cells as well as lung resident CD4 T cells induced after tuberculosis infection (Moguche et al., 2015; Moore et al., 2011). Our data reveal significant transcriptional similarity between TFH memory cells and resident memory T cells, consistent with the non-circulating, tissue-resident characteristics of both subsets (Figure S2G). ICOS blocking leads to downregulation of mTOR signaling and residency gene expression in TFH memory cells (Figure 7D). Given that both TFH and tissue resident memory cells depend on mTOR signals for their generation, it will be interesting to determine if ICOS and mTOR signals are also required to sustain resident memory T cells following acute infection (Sowell et al., 2014; Yang et al., 2016; Zeng et al., 2016).

Our data additionally reveal the contribution of TFH memory cells to plasma cell maintenance in the spleen (Figure 7E). One possibility is that persistent antigen fuels the continuous differentiation of memory B cells into plasma cells (Ochsenbein et al., 2000). The observation of decreased NP-specific GL7+ B cells following ICOS blockade is compatible with this idea (Figure 7E). However, we did not see an impact on NP-specific plasmablasts (data not shown), though we cannot exclude that this might be due to technical limitations. Another possibility is that ICOS blocking interferes with the structural organization of the spleen and/or impairment of the plasma cell niche. Plasma cell survival depends on the availability of soluble factors, such as IL-6, IL-21 and BAFF, all of which can be produced by TFH cells (Tangye, 2011). Both CD4 T cells and BAFF were recently identified as key factors specifically supporting the survival of

splenic plasma cells, although the nature of CD4 derived signals was not reported (Thai et al., 2018). In addition, a recent study demonstrated that blood circulating plasma cells in humans express molecules enabling their interaction with TFH cells and promoting their survival in a mechanism involving cell-cell contact (Ramos-Amaya et al., 2015). One way to discriminate the function of TFH memory cells will be to understand where these cells are localized. During the effector phase, TFH cells localize to B cell follicles by interacting with ICOSL expressed by bystander B cells (Shi et al., 2018). If TFH memory cells support the conversion of memory B cells into plasma cells, we would expect this co-localization to continue at late time points after infection. On the other hand, if TFH cells directly provide survival signals to plasma cells, they may be localized in or near to the red pulp. In this scenario, TFH memory cell interactions with CD11c+ ICOSL-expressing antigen presenting cells would be impaired by ICOSL blockade, leading to apoptosis of TFH memory cells (Teichmann et al., 2015).

Finally, our results have implications for protective immunity and vaccine design. Several studies have reported the presence of circulating TFH memory following vaccination or infection, and a clear relationship between the presence of these TFH cells and protective antibody titers exists (He et al., 2013; Hill et al., 2019; Morita et al., 2011; Sage et al., 2014). Consistent with our study, a recent report showed that while circulating TFH cells are predisposed to enter secondary germinal center responses, local TFH cells are superior at promoting plasma cell differentiation (Asrir et al., 2017). Although the persistence of splenic plasma cells has been appreciated for a long time, a role for TFH memory cells in supporting their survival has been largely overlooked, possibly due to the near absence of this population when isolated without NICD-

protector. Taken together, our data reveal the unexpected persistence of TFH memory cells with the capacity for multipotent recall responses and a sustained contribution to long-lived humoral immunity. These findings establish TFH cells as a highly plastic and long-lived component of adaptive immunity, rendering their induction by vaccination an attractive goal.

Experimental Procedures

Mice

Mice were bred and housed under specific pathogen-free conditions at the University Hospital of Basel according to the animal protection law in Switzerland and authorized by the authorities. For all experiments male or female sex-matched mice that were used that were at least 6 weeks old at the time point of infection. The following mouse strains were used: C57BL/6 CD45.2, C57BL/6 CD45.1, Nur77 GFP, T-bet ZsGreen (kindly provided by Jinfang Zhu, NIH, USA), P2X7R$^{-/-}$ (kindly provided by Fabio Grassi, IRB, Switzerland), Bcl6 RFP (kindly provided by Chen Dong, Tsinghua University, China), SMARTA, NIP (Shane Crotty, Scripps, USA).

Viral infection

Mice were infected by intraperitoneal (i.p.) injection with $2x10^5$ focus forming units (FFU) with LCMV Armstrong. In adoptive transfer studies, recipient mice were infected with LCMV Armstrong by i.p. injection with $2x10^5$ on the day following cell transfer. LCMV was grown on BHK-21 cells and titrated on 3T3-cells as described previously (Battegay, 1993).

In vivo treatments

Anti-ICOSL (HK5.3, Bioxcell, #BE0028) treatment was performed by i.p. injection. Each mouse received 4 injections of 100µg every 72 hours. 2-Deoxy-D-glucose (Sigma, #D8375) was supplied in the drinking water for 14 days at a concentration of 6mg/ml. Rapamycin or vehicle control (1% DMSO in PBS) was given daily by i.p. injection of 75µg/kg body weight for 14 days. For BrdU labelling experiment, BrdU was provided in the drinking water at 0.8mg/ml for 12 days.

NICD-protector

Mice were intravenously (i.v.) injected with 25µg commercial (BioLegend, #149802) or 12.5µg homemade of ARTC2.2-blocking nanobody, s+16 (NICD-protector) 15 minutes prior to organ harvest.

Mixed bone marrow chimeras and adoptive transfers

Wild-type (WT) host CD45.1 mice were lethally irradiated with 2 fractionated doses of 500 cGγ and reconstituted with a 1:1 mixture of bone marrow cells from CD45.1 WT and P2X7R$^{-/-}$ CD45.2 donor mice. The reconstitution ability of T- and B cells was assessed at least 6 weeks after reconstitution and before LCMV infection. Adoptive transfer experiments with CD4 Smarta and NIP cells were performed as previously described (Moon et al., 2009).

Quantitative PCR

RNA from sorted cells was isolated with RNAqueous™-Micro Total RNA Isolation Kit (Invitrogen™) and was reverse transcribed to cDNA using either qScript XLT cDNA SuperMix (Quantabio) or iScript™cDNA Synthesis Kit (Bio-Rad). Samples were run on an Applied Biosystems Viia7 Real-time PCR system. Primers used for the indicated genes are listed in the supplementary table.

Isolation of lymphocytes

Single-cell suspensions of cells were prepared from spleens, blood, liver, and bone marrow. Spleens were either mashed and filtered through a 100µm strainer or digested at 37°C for 1 hour using Collagenase D and DNase I. To isolate bone marrow, femur and tibia bones were flushed with a 25G needle followed by filtration through a 100µm strainer. Livers were perfused with PBS and mashed through a 100µm strainer, followed by gradient centrifugation in Percoll. Lymphocytes from the blood were isolated by gradient centrifugation in Ficoll (LSM MP Biomedicals). Erythrocytes were lysed using Ammonium-Chloride-Potassium (ACK) lysis buffer.

Flow cytometry and cell sorting

Isolation of LCMV-specific CD4 T cells was performed by staining single-cell suspensions for 1 hour at room temperature with Ia^b:$NP_{309-328}$ PE or IA^b:GP_{66-77} APC (provided by NIH tetramer core), followed by enrichment and counting (Moon et al., 2009). Anti-CXCR5 BV421 was added at the time of tetramer staining; for p-S6 detection, cells were stained with tetramer for 20 minutes on ice in the presence of

50nM Dasatinib. LCMV-specific B cells were detected as previously described, using a tetramer for NPΔ340 and a Decoy reagent to discriminate PE-specific B cells (Taylor et al., 2012). All other surface staining was performed for 30min on ice in presence of a viability dye. Transcription factor staining was performed by fixation and permeabilization using the eBioscience Foxp3/Transcription Factor staining set. To assess phospho-protein levels, cells were fixed with BD Phosflow Lyse/Fix Buffer for 10 min at 37°C and permeabilized using BD Phosflow Perm/Wash Buffer for 30 min at room temperature. To stain for BrdU incorporation, the FITC BrdU Flow kit (BD) was used. 2-NBDG staining (Thermo Fisher) was performed for 10 min at 37°C in 100μM 2-NBDG. Fortessa LSR II and Sorp Aria cytometers (BD Biosciences) were used for flow cytometry and cell sorting respectively. Data were analyzed with FlowJo X software (TreeStar).

The following antibodies were used for staining: CD4 (BUV496, GK1.5, BD, #564667), CD8a (biotin, 53-6.7, BioLegend, #100704), CD11b (PE-Cy5, M1/70, BioLegend, #101222), CD11c (PE-Cy5, N418, BioLegend, #117316), CD27 (BV510, LG.3A10, BioLegend, #124229), CD38 (BV421, 90, BD, #562768), CD44 (BUV395, IM7, BD, #740215; APC-Cy7, IM7, BioLegend, #103028; PE, IM7, BD, #553134), CD45.1 (PE, A20, BioLegend, #110707; FITC, A20, BD, #553775), CD45.2 (FITC, 104, BD, #553772; APC-eFluor780, 104, eBioscience, #47-0454-82; APC-Fire, 104, BioLegend, #109852), CD62L (APC, MEL-14, BD, #553152; BV711, MEL-14, BioLegend, #104445), CD69 (FITC, H1.2F3, BD, #553236; PE, H1.2F3, eBioscience, #12-0691-83; APC-Cy7, H1.2F3, BioLegend, #104526; BV785, H1.2F3, BioLegend, #104543), CD73

(APC Fire, TY/11.8, BioLegend, #127221), CD80 (PE-Cy7, 16-10A1, BioLegend, #104734), CD138(BV421, 281-2, BioLegend, #142507; BV711, 281-2, BioLegend, #142519), FAS (PE, 15A7, eBioscience, #12-0951-83; FITC, 15A7, BD, #554257), PSGL-1 (BV605, 2PH1, BD, #740384, BUV395, 2PH1, BD, #740273), CXCR4 (BV711, L276F12, BioLegend, #146517), CCR7 (PE, 4B12, BioLegend, #120106), ICOSL (PE, HK5.3, eBioscience, #12-5985-81), ICOS (PE, 7E.17G9, BioLegend, #117406), PD1 (BV785, 29F.1A12, BioLegend, #135225), IgD (BV510, 11-26c.2a, BioLegend, #405723), IgM (BV786, R6-60.2, BD, #564028), Vα2 TCR (FITC, B20.1, eBioscience, #11-5812-82, PE, B20.1, eBioscience, #12-5812-82), Vβ8.3 (FITC, 1B3.3, BD, #553663; PE, 1B3.3, BD, #553664), B220 (PE-Cy5, RA3-6B2, BioLegend, #103210; BV650, RA3-6B2, BioLegend, #103241; PE-Cy7, RA3-6B2, BioLegend, #103222; biotin, RA3-6B2, BD, #553085), CXCR5 (BV421, L138D7, BioLegend, #145512), F4/80 (PE-Cy5, BM8, BioLegend, #123112), FR4 (PE-Cy7, 12A5, BioLegend, #125012, APC-Fire, 12A5, BioLegend, #125013), GL7 (Alexa Fluor 647, GL7, BioLegend, #144606; Alexa Fluor 48, GL7, BioLegend, #144612), GR-1 (PE-Cy5, RB6-8C5, BioLegend, #108410), Ly6C (BV711, HK1.4, BioLegend, #128037; BV510, HK1.4, BioLegend, #128033; FITC, AL-21, BD, #553104), I-Ab (biotin, AF6-120.1, BioLegend, #116404), NK1.1 (biotin, PK136, BioLegend, #553163), P2X7R (PE, 1F11, BioLegend, #148704; PE-Cy7, 1F11, BioLegend, #148707), Bcl6 (PE-Cy7, K112-91, BD, #563582; PE, K112-91, BD, #561522; AF488, K112-91, BD, #561524), FoxP3 (Alexa Fluor 488, 150D, BioLegend, #320012; PE-Cy7, FJK-16s, eBioscience, #25-5773-82), HIF-1a (PE, 241812, R&D Systems, #IC1935P; Alexa FLuor 700, 241812, R&D Systems, #IC1935N), phospho-AKT S473 (Alexa Fluor 647, D9E, Cell Signalling Technology,

#4075S), phospho-S6 S240/244 (Rabbit mAb, , Cell Signalling Technology, #5364S), Goat anti-Rabbit IgG (Alexa Fluor 488, Life technologies, #A11034), TCF1 (PE, S33-966. BD, #564217), Zombie Fixable Viability Dye (Zombie Red, BioLegend, #423110; Zombie Green, BioLegend, #423112).

Enzyme-linked immunosorbent assay

LCMV-specific NP serum antibody titers were determined as previously described (Sommerstein et al., 2015). Briefly, 96-well plates were coated with 100ul of recombinant NP at 3µg/ml in sodium carbonate buffer adjusted to pH 9.6. Plates were blocked with 5% milk in PBS-Tween 0.05% before adding the prediluted sera to the plate. ABTS color reaction was used to detect HRP-coupled goat anti-mouse IgG antibody (Jackson, 115-035-062). Optical density was measured with a Synergy H1 reader (BioTek).

Detection of LCMV NP-specific IgG antibody secreting cells by ELISpot

LCMV NP-specific antibody secreting cells (ASC) were detected as previously described (Schweier et al., 2019). Briefly, 96-well plates were coated with 100ul of recombinant NP at 3µg/ml in PBS. Plates were blocked with cell culture medium before adding pre-diluted single-cell suspension from the bone marrow or the spleen. Cells were incubated for 5h at 37°C before HRP-coupled goat Fcy-specific anti-mouse IgG antibody was added (Jackson, 115-035-008). AEC solution (BD Bioscience) was used to detect ASC. Spots were quantified using an ELISpot reader from AID.

scRNA-seq

Sample preparation: 3-10 x 10^3 LCMV-specific CD4 memory cells ($CD4^+dump^-$ $CD44^+GP66^+$) were loaded for sequencing from either T-bet ZsGreen (1x sample) or wild-type mice (2x biological replicates) day 35 and day 37 post infection onto a 10x Chromium platform. Each sample represents 1-3 mice. Single-cell capture and cDNA and library preparation were performed with a Single Cell 3' v2 Reagent Kit (10× Genomics) according to manufacturer's instructions. Sequencing was performed on one flow-cell of an Illumina NexSeq 500 machine at the Genomics Facility Basel of the ETH Zurich. Paired-end reads were obtained and their quality was assessed with the FastQC tool (version 0.11.5). The length of the first read was 26 nt, composed of individual cells barcodes of 16 nt, and unique molecular identifiers (UMIs) of 10 nt. The length of the second read, composed of the transcript sequence, was 58 nt. The samples in the different wells were identified using sample barcodes of 8 nt.

Sample analysis: Sequencing data was processed using 10X Genomics' cellranger software version 2.1.0, modified to report only primary alignments. Raw molecule info from cellranger was initially filtered leniently, discarding cells with fewer than 100 genes. The resulting UMI matrix was further filtered to keep only cells with log library size > 2.8, log number of features > 2.6, % mitochondrial reads >= 6, % ribosomal protein reads >= 20. Genes with average counts < .005 were removed. Normalization was done using the R package scran's deconvolution method: cells are pre-clustered, normalized within each cluster, and normalized between each cluster. PCA was run on the normalized data. Technical noise within gene expression was modeled using scran, and biologically relevant highly variable genes were calculated

after separating the technical from biological variance, using FDR < 0.05 and biological variance > 0.1. The PCA was denoised to account for the modelled technical variation. Cells were clustered hierarchically using Ward's method on the distance matrix of the PCA. Default dendrogram cut height using the R package dynamicTreeCut resulted in 3 clusters, which also mapped to the highest average silhouette width. The cut height for a finer clustering (7) was chosen based on the next highest local maximum in a plot of average silhouette width. *t*-distributed stochastic neighbor embedding (tSNE) was executed with a perplexity of 30. GSEA between clusters was performed using camera from the limma R package on standard gene set categories as well as sets curated from relevant publications (Ritchie et al., 2015). Subsequent visualization and analysis such as dropout imputation were performed using version 2.3.4 of the Seurat R package. Single-cell regulatory network interference and clustering (SCENIC) was performed using the published workflow on the pySCENIC github repository (Aibar et al., 2017). Monocle2 was run on data filtered and normalized as above, using genes expressed differentially between the clusters as the source of variation for trajectory construction. Ingenuity Pathway Analysis was performed on a list differentially expressed genes (adj P-value < 0.05) in Th1 vs TFH memory cells obtained from in silico bulk RNA Seq data from the 3-cluster version with default settings.

In silico bulk data was generated from three replicates (one without and two with NICD-protector). Replicate, percent mitochondrial reads and percent ribosomal reads each explained < 0.1 % of variance. Counts for each gene were summed by cluster, and data re-normalized using Trimmed Mean of M-Values (TMM). Differential

expression analysis was performed between the most extreme TFH and Th1 clusters using edgeR and limma.

ATAC-seq

Sample preparation: 6.5-7.5 x 10^3 LCMV-specific TFH cells (Ly6C^{lo}PSGL1^{lo}), TH1 cells (Ly6C^{hi}PSGL1^{hi}) were sorted in duplicates from different mice to obtain biologically independent samples 32 days post infection. Naive CD4 cells (CD44^{lo} CD62L^{hi}) were sorted in duplicates and represent technical replicates. Library preparation for sequencing was performed as described previously with an additional clean up step to reduce reads mapping to mitochondrial DNA(Corces et al., 2017). Briefly, sort-purified cells were lysed and tagmented for 30 min at 37°C. DNA was purified using Zymo DNA Clean and Concentrator Kit and amplified for five cycles. Real-time PCR was used to determine the number of additional PCR cycles. DNA was cleaned up using AMpure XP beads at a 1.2 x ratio twice. Sequencing was performed on an Illumina NexSeq 50 machine using 41-bp paired-end run.

Alignment and basic QC: Reads were aligned to the mouse genome (UCSC version mm10) with bowtie2 (version 2.3.2) using options "--maxins 2000 --no-mixed--no-discordant --local --mm". The output was sorted and indexed with samtools (version 1.7) and duplicated reads were marked with picard (version 2.9.2). The read and alignment quality was evaluated using the qQCReport function of the bioconductor package QuasR (R version 3.5.2; Bioconductor version 3.8).

Single sample peak calling: For each group of biological replicates, regions of accessible chromation where called with macs2 (version 2.1.1.20160309) using the

option '-f BAM -g 2652783500 --nomodel --shift -100 --extsize 200 --broad --keep-dup all --qvalue 0.05'. Since the majority of duplicated reads came from mitochondria, the resulting peak lists were cleaned from peaks called in mitochondria and additionally ENCODE blacklist regions. All peaks also required a log-fold change > 1 and FDR < 0.05. The resulting peak lists, one per population, were merge using the function reduce from the GenomicRanges package, requiring at least 250 bases gap for seperate peak calls and a minimum peak width of 100 bases. This merged peak list resulted in 118999 peaks (5.1% genome) across all five populations. The bioconductor package bamsignals was used to generate a counts matrix for the merged peak list.

Across sample normalization and peak calling: Samples from all 5 populations differed in the enrichment of reads within accessible chromatin as compared to genomic background. That this differential enrichment is most likely a (technical) bias can be concluded when comparing ATAC signal of open versus closed promoters where we do not expect a difference in the dynamic range between both states across samples. One possible source of this bias is a differential tagmentation efficiency between samples as previously observed (Denny et al., 2016). However, this sample specific bias also prohibits the direct comparison of log-fold changes across samples. We therefore devised the following normalization strategy for the peak counts. We used "calibrators" for the log-fold-change the ATAC signal in core promoter regions (as measured 500 bases upstream and 200 bases downstream of the TSS using UCSC refGene annotation); this signal shows a clear bimodality on the log-CPM scale separating open from closed promoters. Since the average log-fold change between open and closed promoters should be the same across samples, we tested several normalization

approaches with the aim to equilibrate this average log-fold change across samples. To this end, promoter counts were added to the matrix of peak counts, log-RPKM levels per peak were calculated normalizing for library size as well as region length, and a normalization strategy was applied. Then, a mixture model (function normalmixEM from mixtools R package) was fitted to the subset of normalized promoter levels and the average log-fold change between open and closed promoters was calculated. This strategy showed that cyclic-loess or quantile normalization of the log-RPKM levels led to the best comparability of promoter log-fold changes across all samples. Note that pure scale normalization as with TMM cannot account for the efficiency bias. We choose quantile normalization as the fastest approach to normalize peak counts across all samples. As a byproduct, this strategy also yields a minimal log-RPKM threshold for calling a region accessible (via accessible promoters). We used this threshold to build an indicator matrix classifying each region across all populations into accessible and inaccessible. We only kept peaks which are called accessible in any of the populations by this strategy (n=37862). The quantile normalized log-CPM levels of the filtered peaks were converted to a bioconductor ExpressionSet object and all further differential accessibility analysis was performed with this object. Specifically, the limma package was used to test for differential accessibility between all pairs of populations using functions lmFit and eBayes.

Differential motif analysis using HOMER: Fasta sequences of TH1 and TFH peaks were extracted using functions from the BSgenome, Biostrings and r tracklayer R/Bioconductor packages. These sequences were stratified according to population specific peaks (=open in only one population) and common peaks (= open in both).

Homer (version 4.9) was used to predict known TF motifs (motif database: vertebrates/known.motif) within these sequence sets by running the command 'homer2 known -strand both' with additional setting specifying the specific peaks as foreground and the common peaks as background sequence sets. Differential motif occurance results were visualized using R.

Ingenuity pathway analysis: Ingenuity pathway analysis (Qiagen, version 01-14) was performed on differentially accessible peak regions ($\log_2$ FC > 0.5 and FDR of 0.05) in Th1 vs TFH memory cells with default settings.

Bulk RNA-seq

Sample preparation: 0.5-4.0 x 10^3 GP66-specific TFH cells (Ly6C^{lo}PSGL1^{lo}) were sorted in quadruplicates from individual mice to obtain biologically independent samples from control and αICOSL treated mice. Total RNA was isolated with the PicoPure™ RNA Isolation kit (ThermoFisher, # KIT0202). cDNA and library preparation were performed with a SMART-Seq v4 Ultra Low Input RNA Sequencing Kit (Takara Bio) according to manufacturer's instructions. Sequencing was performed on one flow-cell of an Illumina NexSeq 500 using 38-bp paired-end run.

Sample analysis: Single-end RNA-seq reads were mapped to the mouse genome assembly, version mm10 (analysis set, downloaded from UCSC https://genome.ucsc.edu), with RNA-STAR (Dobin et al., Bioinformatics 2013, version 2.7.0c), with default parameters except for reporting for multi-mappers only one hit in the final alignment files (outSAMmultNmax=1) and filtering reads without evidence in spliced junction table (outFilterType="BySJout").") (Dobin et al., 2013). All subsequent

gene expression data analyses were done within the R software (R Foundation for Statistical Computing, Vienna, Austria). Using Ensembl Genes mRNA coordinates from ensembl version 84 (https://www.ensembl.org) and the featureCounts function from Rsubread package, we quantified gene expression as the number of reads that started within any annotated exon of a gene (Liao et al., 2019). Only genes annotated as "protein_coding" were kept for further analysis. Genes with low expression were filtered out and TMM normalization performed. Filtered data was processed using voomWithQualityWeights from the limma R package before linear modeling. The most significantly differentially expressed genes were consistent with protein expression experiments. Gene set enrichment analysis was performed using limma's cameraPR on standard gene set categories as well as sets curated from relevant publications.

Extracellular metabolic flux analysis

A Seahorse XFe96 metabolic extracellular flux analyzer was used to determine the extracellular acidification rate (ECAR) in mpH/min and the oxygen consumption rate (OCR) in pmol/min. In brief, T-cells were sorted in CD4+CD44+ TFH cells ($Ly6C^{lo}PSGL1^{lo}$) or TH1 cells ($Ly6C^{hi}PSGL1^{hi}$) and seeded ($2x10^5$/well at memory time point or 2.5 $x10^5$/well at effector time point in respective experiments) in serum-free unbuffered RPMI 1640 medium (Sigma-Aldrich # R6504) onto Cell-Tak (#354240, Coring, NY, USA) coated cell plates. Mito Stress test was performed by sequential addition of oligomycin (1 μM; Sigma Aldrich 75351), carbonyl cyanide-4-(trifluoromethoxy)phenylhydrazone (FCCP; 2 μM; Sigma Aldrich C2920) and rotenone

(1 μM; Sigma Aldrich R8875) at the indicated time points. Metabolic parameters were calculated as described previously (Gubser et al., 2013).

Statistical analysis

For statistical analysis between two groups, Prism7 or 8 (GraphPad Software) was used. Unless noted otherwise, statistical significance was determined using unpaired two-tailed Student's t-test. In time course experiments, statistical analysis was performed for each individual timepoint. * = P <0.05, ** = P < 0.01, *** = P <0.001, **** = P < 0.0001, ns = not significant. Error bars show SD centered on the mean unless otherwise indicated.

Table for qPCR primers

Gene	Forward primer	Reverse primer
Igf1R	GCTTCGTTATCCACGACGATG	GAATGGCGGATCTTCACGTAG
Nav2	CAACCTCAGCACGGATGACATC	TTCCTCTCCACCTGTGAGTGCT
Slc43a1	TTCACATGGTCTGGCCTGG	TGTGGTCCAAGGCTAACCC
Tubb2a	CCTCCACCCCTTCTACAACCA	CCAAAACTTAGCGCCGATCT

References

Aibar, S., Gonzalez-Blas, C.B., Moerman, T., Huynh-Thu, V.A., Imrichova, H., Hulselmans, G., Rambow, F., Marine, J.C., Geurts, P., Aerts, J.*, et al.* (2017). SCENIC: single-cell regulatory network inference and clustering. Nat Methods *14*, 1083-1086.
Araki, K., Turner, A.P., Shaffer, V.O., Gangappa, S., Keller, S.A., Bachmann, M.F., Larsen, C.P., and Ahmed, R. (2009). mTOR regulates memory CD8 T-cell differentiation. Nature *460*, 108-112.

Asrir, A., Aloulou, M., Gador, M., Perals, C., and Fazilleau, N. (2017). Interconnected subsets of memory follicular helper T cells have different effector functions. Nat Commun *8*, 847.

Aswad, F., Kawamura, H., and Dennert, G. (2005). High sensitivity of CD4+CD25+ regulatory T cells to extracellular metabolites nicotinamide adenine dinucleotide and ATP: a role for P2X7 receptors. J Immunol *175*, 3075-3083.

Bantug, G.R., Galluzzi, L., Kroemer, G., and Hess, C. (2018). The spectrum of T cell metabolism in health and disease. Nat Rev Immunol *18*, 19-34.

Battegay, M. (1993). [Quantification of lymphocytic choriomeningitis virus with an immunological focus assay in 24 well plates]. ALTEX *10*, 6-14.

Bekkering, S., Arts, R.J.W., Novakovic, B., Kourtzelis, I., van der Heijden, C., Li, Y., Popa, C.D., Ter Horst, R., van Tuijl, J., Netea-Maier, R.T.*, et al.* (2018). Metabolic Induction of Trained Immunity through the Mevalonate Pathway. Cell *172*, 135-146 e139.

Bentebibel, S.E., Lopez, S., Obermoser, G., Schmitt, N., Mueller, C., Harrod, C., Flano, E., Mejias, A., Albrecht, R.A., Blankenship, D.*, et al.* (2013). Induction of ICOS+CXCR3+CXCR5+ TH cells correlates with antibody responses to influenza vaccination. Sci Transl Med *5*, 176ra132.
Boddupalli, C.S., Nair, S., Gray, S.M., Nowyhed, H.N., Verma, R., Gibson, J.A., Abraham, C., Narayan, D., Vasquez, J., Hedrick, C.C.*, et al.* (2016). ABC transporters and NR4A1 identify a quiescent subset of tissue-resident memory T cells. J Clin Invest *126*, 3905-3916.

Borges da Silva, H., Wang, H., Qian, L.J., Hogquist, K.A., and Jameson, S.C. (2019). ARTC2.2/P2RX7 Signaling during Cell Isolation Distorts Function and Quantification of Tissue-Resident CD8(+) T Cell and Invariant NKT Subsets. J Immunol *202*, 2153-2163.

Buenrostro, J.D., Giresi, P.G., Zaba, L.C., Chang, H.Y., and Greenleaf, W.J. (2013). Transposition of native chromatin for fast and sensitive epigenomic profiling of open chromatin, DNA-binding proteins and nucleosome position. Nat Methods *10*, 1213-1218.

Butt, D., Chan, T.D., Bourne, K., Hermes, J.R., Nguyen, A., Statham, A., O'Reilly, L.A., Strasser, A., Price, S., Schofield, P.*, et al.* (2015). FAS Inactivation Releases Unconventional Germinal Center B Cells that Escape Antigen Control and Drive IgE and Autoantibody Production. Immunity *42*, 890-902.

Cheng, S.C., Quintin, J., Cramer, R.A., Shepardson, K.M., Saeed, S., Kumar, V., Giamarellos-Bourboulis, E.J., Martens, J.H., Rao, N.A., Aghajanirefah, A.*, et al.* (2014). mTOR- and HIF-1alpha-mediated aerobic glycolysis as metabolic basis for trained immunity. Science *345*, 1250684.

Cho, S.H., Raybuck, A.L., Blagih, J., Kemboi, E., Haase, V.H., Jones, R.G., and Boothby, M.R. (2019). Hypoxia-inducible factors in CD4(+) T cells promote metabolism, switch cytokine secretion, and T cell help in humoral immunity. Proc Natl Acad Sci U S A *116*, 8975-8984.

Choi, Y.S., Gullicksrud, J.A., Xing, S., Zeng, Z., Shan, Q., Li, F., Love, P.E., Peng, W., Xue, H.H., and Crotty, S. (2015). LEF-1 and TCF-1 orchestrate T(FH) differentiation by regulating differentiation circuits upstream of the transcriptional repressor Bcl6. Nat Immunol *16*, 980-990.

Choi, Y.S., Yang, J.A., Yusuf, I., Johnston, R.J., Greenbaum, J., Peters, B., and Crotty, S. (2013). Bcl6 expressing follicular helper CD4 T cells are fate committed early and have the capacity to form memory. J Immunol *190*, 4014-4026.

Ciucci, T., Vacchio, M.S., Gao, Y., Tomassoni Ardori, F., Candia, J., Mehta, M., Zhao, Y., Tran, B., Pepper, M., Tessarollo, L.*, et al.* (2019). The Emergence and Functional Fitness of Memory CD4(+) T Cells Require the Transcription Factor Thpok. Immunity *50*, 91-105 e104.

Corces, M.R., Trevino, A.E., Hamilton, E.G., Greenside, P.G., Sinnott-Armstrong, N.A., Vesuna, S., Satpathy, A.T., Rubin, A.J., Montine, K.S., Wu, B.*, et al.* (2017). An improved ATAC-seq protocol reduces background and enables interrogation of frozen tissues. Nat Methods *14*, 959-962.

Crawford, A., Angelosanto, J.M., Kao, C., Doering, T.A., Odorizzi, P.M., Barnett, B.E., and Wherry, E.J. (2014). Molecular and transcriptional basis of CD4(+) T cell dysfunction during chronic infection. Immunity *40*, 289-302.

Crotty, S. (2011). Follicular helper CD4 T cells (TFH). Annu Rev Immunol *29*, 621-663.
Crotty, S., and Ahmed, R. (2018). Immune memory and vaccines : great debates (Cold Spring Harbor, New York: Cold Spring Harbor Laboratory Press).

Denny, S.K., Yang, D., Chuang, C.H., Brady, J.J., Lim, J.S., Gruner, B.M., Chiou, S.H., Schep, A.N., Baral, J., Hamard, C.*, et al.* (2016). Nfib Promotes Metastasis through a Widespread Increase in Chromatin Accessibility. Cell *166*, 328-342.

Dimeloe, S., Mehling, M., Frick, C., Loeliger, J., Bantug, G.R., Sauder, U., Fischer, M., Belle, R., Develioglu, L., Tay, S.*, et al.* (2016). The Immune-Metabolic Basis of Effector Memory CD4+ T Cell Function under Hypoxic Conditions. J Immunol *196*, 106-114.
Djuretic, I.M., Levanon, D., Negreanu, V., Groner, Y., Rao, A., and Ansel, K.M. (2007). Transcription factors T-bet and Runx3 cooperate to activate Ifng and silence Il4 in T helper type 1 cells. Nat Immunol *8*, 145-153.

Dobin, A., Davis, C.A., Schlesinger, F., Drenkow, J., Zaleski, C., Jha, S., Batut, P., Chaisson, M., and Gingeras, T.R. (2013). STAR: ultrafast universal RNA-seq aligner. Bioinformatics *29*, 15-21.

Durek, P., Nordstrom, K., Gasparoni, G., Salhab, A., Kressler, C., de Almeida, M., Bassler, K., Ulas, T., Schmidt, F., Xiong, J.*, et al.* (2016). Epigenomic Profiling of Human CD4(+) T Cells Supports a Linear Differentiation Model and Highlights Molecular Regulators of Memory Development. Immunity *45*, 1148-1161.

Fernandez-Ruiz, D., Ng, W.Y., Holz, L.E., Ma, J.Z., Zaid, A., Wong, Y.C., Lau, L.S., Mollard, V., Cozijnsen, A., Collins, N.*, et al.* (2016). Liver-Resident Memory CD8(+) T Cells Form a Front-Line Defense against Malaria Liver-Stage Infection. Immunity *45*, 889-902.

Finlay, D.K., Rosenzweig, E., Sinclair, L.V., Feijoo-Carnero, C., Hukelmann, J.L., Rolf, J., Panteleyev, A.A., Okkenhaug, K., and Cantrell, D.A. (2012). PDK1 regulation of mTOR and hypoxia-inducible factor 1 integrate metabolism and migration of CD8+ T cells. J Exp Med *209*, 2441-2453.

Gubser, P.M., Bantug, G.R., Razik, L., Fischer, M., Dimeloe, S., Hoenger, G., Durovic, B., Jauch, A., and Hess, C. (2013). Rapid effector function of memory CD8+ T cells requires an immediate-early glycolytic switch. Nat Immunol *14*, 1064-1072.
Hale, J.S., and Ahmed, R. (2015). Memory T follicular helper CD4 T cells. Front Immunol *6*, 16.

Hale, J.S., Youngblood, B., Latner, D.R., Mohammed, A.U., Ye, L., Akondy, R.S., Wu, T., Iyer, S.S., and Ahmed, R. (2013). Distinct Memory CD4(+) T Cells with Commitment to T Follicular Helper- and T Helper 1-Cell Lineages Are Generated after Acute Viral Infection. Immunity *38*, 805-817.

He, J., Tsai, L.M., Leong, Y.A., Hu, X., Ma, C.S., Chevalier, N., Sun, X., Vandenberg, K., Rockman, S., Ding, Y.*, et al.* (2013). Circulating precursor CCR7(lo)PD-1(hi) CXCR5(+) CD4(+) T cells indicate Tfh cell activity and promote antibody responses upon antigen reexposure. Immunity *39*, 770-781.

Heinz, S., Benner, C., Spann, N., Bertolino, E., Lin, Y.C., Laslo, P., Cheng, J.X., Murre, C., Singh, H., and Glass, C.K. (2010). Simple combinations of lineage-determining transcription factors prime cis-regulatory elements required for macrophage and B cell identities. Mol Cell *38*, 576-589.

Hendriks, J., Gravestein, L.A., Tesselaar, K., van Lier, R.A., Schumacher, T.N., and Borst, J. (2000). CD27 is required for generation and long-term maintenance of T cell immunity. Nat Immunol *1*, 433-440.

Hill, D.L., Pierson, W., Bolland, D.J., Mkindi, C., Carr, E.J., Wang, J., Houard, S., Wingett, S.W., Audran, R., Wallin, E.F.*, et al.* (2019). The adjuvant GLA-SE promotes human Tfh cell expansion and emergence of public TCRbeta clonotypes. J Exp Med.
Homann, D., Teyton, L., and Oldstone, M.B. (2001). Differential regulation of antiviral T-cell immunity results in stable CD8+ but declining CD4+ T-cell memory. Nat Med *7*, 913-919.

Hombrink, P., Helbig, C., Backer, R.A., Piet, B., Oja, A.E., Stark, R., Brasser, G., Jongejan, A., Jonkers, R.E., Nota, B.*, et al.* (2016). Programs for the persistence, vigilance and control of human CD8(+) lung-resident memory T cells. Nat Immunol *17*, 1467-1478.

Hubert, S., Rissiek, B., Klages, K., Huehn, J., Sparwasser, T., Haag, F., Koch-Nolte, F., Boyer, O., Seman, M., and Adriouch, S. (2010). Extracellular NAD+ shapes the Foxp3+ regulatory T cell compartment through the ART2-P2X7 pathway. J Exp Med *207*, 2561-2568.

Iyer, S.S., Latner, D.R., Zilliox, M.J., McCausland, M., Akondy, R.S., Penaloza-Macmaster, P., Hale, J.S., Ye, L., Mohammed, A.U., Yamaguchi, T.*, et al.* (2013). Identification of novel markers for mouse CD4(+) T follicular helper cells. Eur J Immunol *43*, 3219-3232.

Karmaus, P.W.F., Chen, X., Lim, S.A., Herrada, A.A., Nguyen, T.M., Xu, B., Dhungana, Y., Rankin, S., Chen, W., Rosencrance, C.*, et al.* (2019). Metabolic heterogeneity underlies reciprocal fates of TH17 cell stemness and plasticity. Nature *565*, 101-105.
Keck, S., Schmaler, M., Ganter, S., Wyss, L., Oberle, S., Huseby, E.S., Zehn, D., and King, C.G. (2014). Antigen affinity and antigen dose exert distinct influences on CD4 T-cell differentiation. Proc Natl Acad Sci U S A *111*, 14852-14857.

Kohu, K., Ohmori, H., Wong, W.F., Onda, D., Wakoh, T., Kon, S., Yamashita, M., Nakayama, T., Kubo, M., and Satake, M. (2009). The Runx3 transcription factor augments Th1 and down-modulates Th2 phenotypes by interacting with and attenuating GATA3. J Immunol *183*, 7817-7824.

Kramer, A., Green, J., Pollard, J., Jr., and Tugendreich, S. (2014). Causal analysis approaches in Ingenuity Pathway Analysis. Bioinformatics *30*, 523-530.
Lau, C.M., Adams, N.M., Geary, C.D., Weizman, O.E., Rapp, M., Pritykin, Y., Leslie, C.S., and Sun, J.C. (2018). Epigenetic control of innate and adaptive immune memory. Nat Immunol *19*, 963-972.

Liao, Y., Smyth, G.K., and Shi, W. (2019). The R package Rsubread is easier, faster, cheaper and better for alignment and quantification of RNA sequencing reads. Nucleic Acids Res.

Luthje, K., Kallies, A., Shimohakamada, Y., Belz, G.T., Light, A., Tarlinton, D.M., and Nutt, S.L. (2012). The development and fate of follicular helper T cells defined by an IL-21 reporter mouse. Nat Immunol *13*, 491-498.

Ma, C.S., Avery, D.T., Chan, A., Batten, M., Bustamante, J., Boisson-Dupuis, S., Arkwright, P.D., Kreins, A.Y., Averbuch, D., Engelhard, D.*, et al.* (2012). Functional STAT3 deficiency compromises the generation of human T follicular helper cells. Blood *119*, 3997-4008.

Mackay, L.K., Minnich, M., Kragten, N.A., Liao, Y., Nota, B., Seillet, C., Zaid, A., Man, K., Preston, S., Freestone, D.*, et al.* (2016). Hobit and Blimp1 instruct a universal transcriptional program of tissue residency in lymphocytes. Science *352*, 459-463.
Mackay, L.K., Rahimpour, A., Ma, J.Z., Collins, N., Stock, A.T., Hafon, M.L., Vega-Ramos, J., Lauzurica, P., Mueller, S.N., Stefanovic, T.*, et al.* (2013). The developmental pathway for CD103(+)CD8+ tissue-resident memory T cells of skin. Nat Immunol *14*, 1294-1301.

Maekawa, Y., Ishifune, C., Tsukumo, S., Hozumi, K., Yagita, H., and Yasutomo, K. (2015). Notch controls the survival of memory CD4+ T cells by regulating glucose uptake. Nat Med *21*, 55-61.

Majchrzak, K., Nelson, M.H., Bowers, J.S., Bailey, S.R., Wyatt, M.M., Wrangle, J.M., Rubinstein, M.P., Varela, J.C., Li, Z., Himes, R.A.*, et al.* (2017). beta-catenin and PI3Kdelta inhibition expands precursor Th17 cells with heightened stemness and antitumor activity. JCI Insight *2*.

Marshall, H.D., Chandele, A., Jung, Y.W., Meng, H., Poholek, A.C., Parish, I.A., Rutishauser, R., Cui, W., Kleinstein, S.H., Craft, J., and Kaech, S.M. (2011). Differential expression of Ly6C and T-bet distinguish effector and memory Th1 CD4(+) cell properties during viral infection. Immunity *35*, 633-646.

Marshall, H.D., Ray, J.P., Laidlaw, B.J., Zhang, N., Gawande, D., Staron, M.M., Craft, J., and Kaech, S.M. (2015). The transforming growth factor beta signaling pathway is critical for the formation of CD4 T follicular helper cells and isotype-switched antibody responses in the lung mucosa. Elife *4*, e04851.

Martinez, G.J., Pereira, R.M., Aijo, T., Kim, E.Y., Marangoni, F., Pipkin, M.E., Togher, S., Heissmeyer, V., Zhang, Y.C., Crotty, S.*, et al.* (2015). The transcription factor NFAT promotes exhaustion of activated CD8(+) T cells. Immunity *42*, 265-278.
Moguche, A.O., Shafiani, S., Clemons, C., Larson, R.P., Dinh, C., Higdon, L.E., Cambier, C.J., Sissons, J.R., Gallegos, A.M., Fink, P.J., and Urdahl, K.B. (2015). ICOS

and Bcl6-dependent pathways maintain a CD4 T cell population with memory-like properties during tuberculosis. J Exp Med *212*, 715-728.

Moon, H., Na, H.Y., Chong, K.H., and Kim, T.J. (2006). P2X7 receptor-dependent ATP-induced shedding of CD27 in mouse lymphocytes. Immunol Lett *102*, 98-105.
Moon, J.J., Chu, H.H., Hataye, J., Pagan, A.J., Pepper, M., McLachlan, J.B., Zell, T., and Jenkins, M.K. (2009). Tracking epitope-specific T cells. Nat Protoc *4*, 565-581.
Moore, T.V., Clay, B.S., Ferreira, C.M., Williams, J.W., Rogozinska, M., Cannon, J.L., Shilling, R.A., Marzo, A.L., and Sperling, A.I. (2011). Protective effector memory CD4 T cells depend on ICOS for survival. PLoS One *6*, e16529.

Morita, R., Schmitt, N., Bentebibel, S.E., Ranganathan, R., Bourdery, L., Zurawski, G., Foucat, E., Dullaers, M., Oh, S., Sabzghabaei, N.*, et al.* (2011). Human blood CXCR5(+)CD4(+) T cells are counterparts of T follicular cells and contain specific subsets that differentially support antibody secretion. Immunity *34*, 108-121.

Moskowitz, D.M., Zhang, D.W., Hu, B., Le Saux, S., Yanes, R.E., Ye, Z., Buenrostro, J.D., Weyand, C.M., Greenleaf, W.J., and Goronzy, J.J. (2017). Epigenomics of human CD8 T cell differentiation and aging. Sci Immunol *2*.

Muranski, P., Borman, Z.A., Kerkar, S.P., Klebanoff, C.A., Ji, Y., Sanchez-Perez, L., Sukumar, M., Reger, R.N., Yu, Z., Kern, S.J.*, et al.* (2011). Th17 cells are long lived and retain a stem cell-like molecular signature. Immunity *35*, 972-985.

Nance, J.P., Belanger, S., Johnston, R.J., Takemori, T., and Crotty, S. (2015). Cutting edge: T follicular helper cell differentiation is defective in the absence of Bcl6 BTB repressor domain function. J Immunol *194*, 5599-5603.

Ndungu, F.M., Cadman, E.T., Coulcher, J., Nduati, E., Couper, E., Macdonald, D.W., Ng, D., and Langhorne, J. (2009). Functional memory B cells and long-lived plasma cells are generated after a single Plasmodium chabaudi infection in mice. PLoS Pathog *5*, e1000690.

Ochsenbein, A.F., Pinschewer, D.D., Sierro, S., Horvath, E., Hengartner, H., and Zinkernagel, R.M. (2000). Protective long-term antibody memory by antigen-driven and T help-dependent differentiation of long-lived memory B cells to short-lived plasma cells independent of secondary lymphoid organs. Proc Natl Acad Sci U S A *97*, 13263-13268.

Oxenius, A., Bachmann, M.F., Zinkernagel, R.M., and Hengartner, H. (1998). Virus-specific MHC-class II-restricted TCR-transgenic mice: effects on humoral and cellular immune responses after viral infection. Eur J Immunol *28*, 390-400.

Pearce, E.L., Walsh, M.C., Cejas, P.J., Harms, G.M., Shen, H., Wang, L.S., Jones, R.G., and Choi, Y. (2009). Enhancing CD8 T-cell memory by modulating fatty acid metabolism. Nature *460*, 103-107.

Pepper, M., Linehan, J.L., Pagan, A.J., Zell, T., Dileepan, T., Cleary, P.P., and Jenkins, M.K. (2010). Different routes of bacterial infection induce long-lived TH1 memory cells and short-lived TH17 cells. Nat Immunol *11*, 83-89.

Pepper, M., Pagan, A.J., Igyarto, B.Z., Taylor, J.J., and Jenkins, M.K. (2011). Opposing signals from the Bcl6 transcription factor and the interleukin-2 receptor generate T helper 1 central and effector memory cells. Immunity *35*, 583-595.

Phan, A.T., Doedens, A.L., Palazon, A., Tyrakis, P.A., Cheung, K.P., Johnson, R.S., and Goldrath, A.W. (2016). Constitutive Glycolytic Metabolism Supports CD8(+) T Cell Effector Memory Differentiation during Viral Infection. Immunity *45*, 1024-1037.

Proietti, M., Cornacchione, V., Rezzonico Jost, T., Romagnani, A., Faliti, C.E., Perruzza, L., Rigoni, R., Radaelli, E., Caprioli, F., Preziuso, S.*, et al.* (2014). ATP-gated ionotropic P2X7 receptor controls follicular T helper cell numbers in Peyer's patches to promote host-microbiota mutualism. Immunity *41*, 789-801.

Ray, J.P., Staron, M.M., Shyer, J.A., Ho, P.C., Marshall, H.D., Gray, S.M., Laidlaw, B.J., Araki, K., Ahmed, R., Kaech, S.M., and Craft, J. (2015). The Interleukin-2-mTORc1 Kinase Axis Defines the Signaling, Differentiation, and Metabolism of T Helper 1 and Follicular B Helper T Cells. Immunity *43*, 690-702.

Ritchie, M.E., Phipson, B., Wu, D., Hu, Y., Law, C.W., Shi, W., and Smyth, G.K. (2015). limma powers differential expression analyses for RNA-sequencing and microarray studies. Nucleic Acids Res *43*, e47.

Saeed, S., Quintin, J., Kerstens, H.H., Rao, N.A., Aghajanirefah, A., Matarese, F., Cheng, S.C., Ratter, J., Berentsen, K., van der Ent, M.A.*, et al.* (2014). Epigenetic programming of monocyte-to-macrophage differentiation and trained innate immunity. Science *345*, 1251086.

Sage, P.T., Alvarez, D., Godec, J., von Andrian, U.H., and Sharpe, A.H. (2014). Circulating T follicular regulatory and helper cells have memory-like properties. J Clin Invest *124*, 5191-5204.

Satija, R., Farrell, J.A., Gennert, D., Schier, A.F., and Regev, A. (2015). Spatial reconstruction of single-cell gene expression data. Nat Biotechnol *33*, 495-502.
Schweier, O., Aichele, U., Marx, A.F., Straub, T., Verbeek, J.S., Pinschewer, D.D., and Pircher, H. (2019). Residual LCMV antigen in transiently CD4(+) T cell-depleted mice induces high levels of virus-specific antibodies but only limited B-cell memory. Eur J Immunol *49*, 626-637.

Shi, J., Hou, S., Fang, Q., Liu, X., Liu, X., and Qi, H. (2018). PD-1 Controls Follicular T Helper Cell Positioning and Function. Immunity *49*, 264-274 e264.

Siegel, A.M., Heimall, J., Freeman, A.F., Hsu, A.P., Brittain, E., Brenchley, J.M., Douek, D.C., Fahle, G.H., Cohen, J.I., Holland, S.M., and Milner, J.D. (2011). A critical role for STAT3 transcription factor signaling in the development and maintenance of human T cell memory. Immunity *35*, 806-818.

Slifka, M.K., and Ahmed, R. (1996). Long-term antibody production is sustained by antibody-secreting cells in the bone marrow following acute viral infection. Ann N Y Acad Sci *797*, 166-176.

Slifka, M.K., Antia, R., Whitmire, J.K., and Ahmed, R. (1998). Humoral immunity due to long-lived plasma cells. Immunity *8*, 363-372.

Slifka, M.K., Matloubian, M., and Ahmed, R. (1995). Bone marrow is a major site of long-term antibody production after acute viral infection. J Virol *69*, 1895-1902.
Sommerstein, R., Flatz, L., Remy, M.M., Malinge, P., Magistrelli, G., Fischer, N., Sahin, M., Bergthaler, A., Igonet, S., Ter Meulen, J.*, et al.* (2015). Arenavirus Glycan Shield Promotes Neutralizing Antibody Evasion and Protracted Infection. PLoS Pathog *11*, e1005276.

Sowell, R.T., Rogozinska, M., Nelson, C.E., Vezys, V., and Marzo, A.L. (2014). Cutting edge: generation of effector cells that localize to mucosal tissues and form resident memory CD8 T cells is controlled by mTOR. J Immunol *193*, 2067-2071.

Tangye, S.G. (2011). Staying alive: regulation of plasma cell survival. Trends Immunol *32*, 595-602.

Taylor, J.J., Pape, K.A., and Jenkins, M.K. (2012). A germinal center-independent pathway generates unswitched memory B cells early in the primary response. J Exp Med *209*, 597-606.

Teichmann, L.L., Cullen, J.L., Kashgarian, M., Dong, C., Craft, J., and Shlomchik, M.J. (2015). Local triggering of the ICOS coreceptor by CD11c(+) myeloid cells drives organ inflammation in lupus. Immunity *42*, 552-565.

Thai, L.H., Le Gallou, S., Robbins, A., Crickx, E., Fadeev, T., Zhou, Z., Cagnard, N., Megret, J., Bole, C., Weill, J.C.*, et al.* (2018). BAFF and CD4(+) T cells are major survival factors for long-lived splenic plasma cells in a B-cell-depletion context. Blood *131*, 1545-1555.

Tian, Y., Babor, M., Lane, J., Schulten, V., Patil, V.S., Seumois, G., Rosales, S.L., Fu, Z., Picarda, G., Burel, J.*, et al.* (2017). Unique phenotypes and clonal expansions of human CD4 effector memory T cells re-expressing CD45RA. Nat Commun *8*, 1473.
Trapnell, C., Cacchiarelli, D., Grimsby, J., Pokharel, P., Li, S., Morse, M., Lennon, N.J., Livak, K.J., Mikkelsen, T.S., and Rinn, J.L. (2014). The dynamics and regulators of cell fate decisions are revealed by pseudotemporal ordering of single cells. Nat Biotechnol *32*, 381-386.

Tubo, N.J., Pagan, A.J., Taylor, J.J., Nelson, R.W., Linehan, J.L., Ertelt, J.M., Huseby, E.S., Way, S.S., and Jenkins, M.K. (2013). Single Naive CD4(+) T Cells from a Diverse Repertoire Produce Different Effector Cell Types during Infection. Cell *153*, 785-796.
Utzschneider, D.T., Charmoy, M., Chennupati, V., Pousse, L., Ferreira, D.P., Calderon-Copete, S., Danilo, M., Alfei, F., Hofmann, M., Wieland, D.*, et al.* (2016). T Cell Factor 1-Expressing Memory-like CD8(+) T Cells Sustain the Immune Response to Chronic Viral Infections. Immunity *45*, 415-427.

Weber, J.P., Fuhrmann, F., Feist, R.K., Lahmann, A., Al Baz, M.S., Gentz, L.J., Vu Van, D., Mages, H.W., Haftmann, C., Riedel, R.*, et al.* (2015). ICOS maintains the T follicular helper cell phenotype by down-regulating Kruppel-like factor 2. J Exp Med *212*, 217-233.

Williams, M.A., Ravkov, E.V., and Bevan, M.J. (2008). Rapid culling of the CD4+ T cell repertoire in the transition from effector to memory. Immunity *28*, 533-545.

Wing, J.B., Kitagawa, Y., Locci, M., Hume, H., Tay, C., Morita, T., Kidani, Y., Matsuda, K., Inoue, T., Kurosaki, T.*, et al.* (2017). A distinct subpopulation of CD25(-) T-follicular regulatory cells localizes in the germinal centers. Proc Natl Acad Sci U S A *114*, E6400-E6409.

Wu, J.Q., Seay, M., Schulz, V.P., Hariharan, M., Tuck, D., Lian, J., Du, J., Shi, M., Ye, Z., Gerstein, M.*, et al.* (2012). Tcf7 is an important regulator of the switch of self-renewal and differentiation in a multipotential hematopoietic cell line. PLoS Genet *8*, e1002565.
Xu, L., Huang, Q., Wang, H., Hao, Y., Bai, Q., Hu, J., Li, Y., Wang, P., Chen, X., He, R.*, et al.* (2017). The Kinase mTORC1 Promotes the Generation and Suppressive Function of Follicular Regulatory T Cells. Immunity *47*, 538-551 e535.

Yang, J., Lin, X., Pan, Y., Wang, J., Chen, P., Huang, H., Xue, H.H., Gao, J., and Zhong, X.P. (2016). Critical roles of mTOR Complex 1 and 2 for T follicular helper cell differentiation and germinal center responses. Elife *5*.

Ye, L., Lee, J., Xu, L., Mohammed, A.U., Li, W., Hale, J.S., Tan, W.G., Wu, T., Davis, C.W., Ahmed, R., and Araki, K. (2017). mTOR Promotes Antiviral Humoral Immunity by Differentially Regulating CD4 Helper T Cell and B Cell Responses. J Virol *91*.

Zaiss, D.M.W., Gause, W.C., Osborne, L.C., and Artis, D. (2015). Emerging functions of amphiregulin in orchestrating immunity, inflammation, and tissue repair. Immunity *42*, 216-226.

Zeng, H., Cohen, S., Guy, C., Shrestha, S., Neale, G., Brown, S.A., Cloer, C., Kishton, R.J., Gao, X., Youngblood, B.*, et al.* (2016). mTORC1 and mTORC2 Kinase Signaling and Glucose Metabolism Drive Follicular Helper T Cell Differentiation. Immunity *45*, 540-554.

Zhu, Y., Zhao, Y., Zou, L., Zhang, D., Aki, D., and Liu, Y.C. (2019). The E3 ligase VHL promotes follicular helper T cell differentiation via glycolytic-epigenetic control. J Exp Med.

Author contributions

Conceptualization, CK, MK, DS; Methodology, MK, DS, CK; Investigation, MK, TP, CK, JL, NS; Formal analysis, MK, DS, CK, JR, FG; Software, DS, JR, FG; Writing - CK, DS, MK; Visualization, DS, MK, CK; Funding acquisition, CK; Resources, DP, JT, CH; Supervision, CK

Acknowledgements

We thank D.Pinschewer for many helpful discussions, sharing reagents and technical advice, M. Linterman for critical reading of the manuscript, G.Bantug and D.Labes for expertise and discussion, C. Beisel for technical advice, R.Tussiwand and her lab for feedback and support; the flow sorting facility and all the animal caretakers at the DBM University of Basel. Single-cell RNA-sequencing was performed at the Genomics Facility Basel, ETH Zurich. Calculations were performed at sciCORE (http://scicore.unibas.ch/) scientific computing center at the University of Basel. The work was supported by research grants to CGK (SNF PP00P3_157520, Gottfried and Julia Bangerter-Rhyner Stiftung, Olga Mayenfisch Stiftung and Swiss Life Jubiläumsstiftung).

Main Figure Legends

Figure 1 | TFH memory cells are long-lived but susceptible to NAD induced cell death during isolation

(A) Flow cytometry analysis of GP66-specific CD4 T cells isolated from the spleen at the indicated time points post infection, with or without NICD-protector using different gating strategies to identify TFH memory cells (Ly6C^{lo}PSGL1^{lo} or CXCR5^{hi}PD1^{hi} or FR4^{hi}Ly6C^{lo}).

(B) tSNE plots of the GP66-specific CD4 memory compartment with (middle, right) or without NICD-protector (left) and overlaid P2X7R expression (right).

(C) Quantification of GP66-specific Th1 (red, Ly6C^{hi}PSGL1^{hi}) or TFH memory cells (blue, Ly6C^{lo}PSGL1^{lo}) numbers over time with (solid line) or without (dashed line) NICD-protector gated as in Figure 1D. Thin lines represent the mean + s.d. (*n* = 3-4 mice per group).

(D-E), Representative flow cytometry plots (D) and mean fluorescence intensity (MFI) (E) of the indicated marker in GP66- specific CD4 memory cell subsets Th1 (red), TCM (green), and TFH (blue) >40 days post infection. Data represent at least *n* = 2 independent experiments with a minimum number of 3 mice per group.

Figure 2 TFH memory cells are transcriptionally distinct from TCM

(A) Unsupervised hierarchical clustering using Ward's method: PCA and tSNE dimension reductions.

(B) Heatmap showing scaled, centered single cell expression data of top 10 cluster-defining genes by cluster.

(C-E) Log-normalized expression of genes typical for TFH (C), TCM (D) and Th1 (E)

populations.

(F) Log-normalized average expression of published CD4 signatures obtained by analysis of d7 effectors: TFH, TCM precursors, and Th1.

(G) scRNA-seq: Rank of Ccr7 and Izumo1r (encoding FR4) among Spearman's rank correlation coefficients between Cxcr5 and all other genes.

(H) scRNA-seq: Cxcr5 vs Ccr7 on imputed data, colored by cluster. Dropout imputed using Seurat::AddImputedScore unless otherwise noted.

(I) Scaled, centered single cell expression of Izumo1r in comparison to other common gating markers. Unless otherwise noted, scRNA-seq data are shown from the run with NICD-protector to ensure consistency with other experiments.

(J) Flow cytometric analysis of CCR7, CXCR5 and FR4 on GP-66 specific CD4 memory cells >50 days post infection gated as in Figure 1D.

Figure 3 | TFH memory cells are constitutively glycolytic

(A) Empirical cumulative distribution of scaled, centered mRNA expression by cluster of Rptor-regulated genes (above) (Zeng et al., 2016) and the gene set HALLMARK_GLYCOLYSIS (below).

(B) quantitative PCR of indicated genes (arbitrary units (AU) relative to Rpl13a) in sort-purified GP66-specific Th1 (red, Ly6C^{hi}PSGL1^{hi}), TCM (green, Ly6C^{lo}PSGL1^{hi}) and TFH (blue, Ly6C^{lo}PSGL-1^{lo}) CD4 memory cells. Data is representative of *n*= 2 independent experiments depicting the mean +s.d. of three technical replicates.

(C-D) Representative flow cytometry histograms and MFI from one experiment of intracellular phospho-S6 Ser240/244 on CD44+CD4 Th1 (red) or TFH (blue) memory

cells compared to naive CD4 T cells (grey histogram) (C) and 2-NBDG uptake (D) on GP66-specific CD4 memory cells >30 days post infection compared to FMO control (grey histogram) with *n* = 2 independent experiments (each dot represents cells from individual mice, and the thin line represents the mean).

(E) Quantification of basal ECAR (left) and ECAR profile (right) in response to oligomycin (oligo), fluoro-carbonyl cyanide phenylhydrazone (FCCP), rotenone (Rot) in sort purified Th1 (red, Ly6C^{hi}PSGL1^{hi}) and TFH (blue, Ly6C^{lo}PSGL-1^{lo}) CD4 memory cells pooled from 20-30 mice. Data are representative of *n* = 2 independent experiments.

(F-G) Representative plots (F) of flow cytometric analysis of GP66-specific CD4 memory cells treated with vehicle or 2-DG/ Rapamycin of *n* = 2 independent experiments and cell numbers and proportions of GP66-specific TFH memory cells using either Ly6C^{lo}PSGL1^{lo} or CXCR5^{hi}PD1^{hi} as gating strategy (G). Each dot represents cells from individual mice, and the thin line represents the mean.

(H) P2X7R$^{-/-}$ to wildtype ratio of GP66-specific CD4 memory cells in BM chimera mice >60 days post infection compared to ratio of total CD4 compartment after reconstitution Data represent n = 2 independent experiments with each dot and connecting line represents one individual mouse.

(I) Flow cytometric analysis of GP66-specific CD4 memory cells in P2X7R-/- or wildtype compartment using either Ly6CloPSGL1lo or CXCR5hiPD1hi as gating strategy to identify TFH memory cells >60 days post infection.

Figure 4 | TFH memory cells can survive in the absence of antigen

(A) Flow cytometry analysis of Nur77 expression by GP66-specific TFH memory cells for the indicated gating strategies.

(B) Representative flow cytometry plots (left panels) and MFI (right panel) depicting PD1 expression on Nur77+ (dotted blue line) and Nur77- (tinted blue line) TFH cells, gated as depicted in panel (A).

(C) Flow cytometry plots (left) and quantification (right) of BrdU incorporation by GP66-specific CD4 memory subsets.

(D-E) Total GP66-specific CD4 T cells were isolated at day 10 after LCMV infection and transferred into congenic infection matched (LCMV) or naive mice. Donor cell phenotype was analyzed at day 30 after infection. Representative flow cytometry plots (D) and quantification (E) with gating for PSGL1^{lo}Ly6C^{lo} (left), PD1^{hi}CXCR5^{hi} (middle) and PSGL1^{lo}FR4^{hi} (right). Data represent *n* = 2 independent experiments and each dot represents cells from individual mice, and the line marks the mean.

Figure 5 | TFH memory cells give rise to multiple cell fates upon recall

(A) Log-normalized average expression of genes tracking with Tcf7 (Utzschneider et al., 2016).

(B) Flow cytometry analysis of TCF1(left) and MFI (right) in Th1 (red), Ly6C^{lo} Th1 (green) and TFH (blue) GP66-specific memory cells. Data represents *n* = 2 independent experiments with 5 mice each.

(C) Density of cells in pseudotime, Monocle2 analysis.

(D) GP66-specific Ly6C^{hi} Th1, Ly6C^{lo} Th1 or TFH CD4 memory T cells were sorted at day 35-45 after LCMV infection and transferred into congenic naive mice. The recipient mice were challenged with LCMV the following day. Donor cell phenotype was analyzed at day 12 after infection.

(E) Representative plots of flow cytometric analysis of Ly6C^{hi} Th1 (red), Ly6C^{lo} Th1 (green) or TFH (blue) donor cell phenotype.

(F) Quantification of Ly6C^{hi} Th1 effectors (red), Ly6C^{lo} Th1(green) and TFH (blue) effectors from Ly6C^{hi} Th1, Ly6C^{lo} Th1 or TFH donors compared to endogenous response.

Figure 6 | Epigenetic regulation of TFH memory T cells

(A) PCA of Assay for Transposase-Accessible Chromatin using sequencing (ATAC-seq) data on all peaks.

(B) Heatmap of hierarchically clustered promoter regions with highlighted genes.

(C) Enriched motifs in TFH memory cells found by HOMER.

(D) GSEA analysis of Rptor (above) and Tcf7 (below) regulated genes with negative enrichment score indicating enrichment in TFH memory and positive score indicating enrichment in Th1 memory.

(E) Top 5 pathways enriched in TFH memory cells determined by Ingenuity Pathway Analysis in: combined scRNA-seq data (with and without NICD-protector) comparing TFH cluster to Th1 cluster from 3-cluster version (left) and ATAC-seq peaks mapped to nearest TSS within TAD (right).

Figure 7 | ICOS signaling integrates TFH memory cell stemness and metabolism and contributes to late phase humoral immune responses

(A) Mice were infected with LCMV followed by anti-ICOSL treatment at late time points after infection. LCMV specific CD4 T cells and B cells were analyzed after 12 days of treatment.

(B) Cell numbers of GP66-specific TFH memory cells in treated mice using either Ly6C^{lo}PSGL1^{lo} or CXCR5^{hi}PD1^{hi} as gating strategy. Data represents one of *n* = 2 independent experiments.

(C) Scaled, centered expression of 20 most significant differentially expressed transcripts in TFH memory cells between control and anti-ICOSL treated mice.

(D) Most significantly downregulated gene signatures with anti-ICOSL blocking (FDR < 0.2) (Boddupalli et al., 2016; Choi et al., 2015; Ciucci et al., 2019; Crawford et al., 2014; Hale et al., 2013; Martinez et al., 2015; Wing et al., 2017; Wu et al., 2012; Zeng et al., 2016).

(E) NP-specific IgG serum titer (far left), numbers of NP-specific GL7+ B cells (left) and NP-specific antibody secreting cells from the spleen (right) and bone marrow (far right). Data summarize *n* = 2 independent experiments with dots representing individual mice and bars indicating the mean.

Supplementary Figure Legends

Supplementary Figure 1 | TFH memory cells are susceptible to NAD induced cell death

(A) Flow cytometry analysis of GP66-specific CD4 T cells isolated from the spleen at day 15 post infection, with or without NICD-protector comparing the GP66 epitope to the NP epitope. Different gating strategies were used to identify TFH memory cells (PSGL1^{lo}Ly6C^{lo} or PD1^{hi}CXCR5^{hi} or Ly6C^{lo}FR4^{hi}).

(B) Comparison of total epitope-specific CD4 memory cell numbers in control and NICD-protector treated mice >30 days post infection (each dot represents cells from individual mice, and the thin line represents the mean).

(C) Quantification of GP66-specific Ly6C^{lo} Th1 memory cells (green, Ly6C^{lo}PSGL1^{hi} gated as in Fig 1D over time with (solid line) or without (dashed line) NICD-protector. Thin lines represent the mean + s.d. (*n* = 3-4 mice per group).

(D) Representative flow cytometry plots (left) and proportions of TFH memory cells (right) in TCR-transgenic Smarta and NIP memory cells compared to polyclonal GP66-specific and NP-specific CD4 memory compartment >30 days post infection. Data smmarize *n* = 2 independent experiments for each group (each dot represents cells from individual mice, and the line represents the mean).

Supplementary Figure 2 | TFH memory cells are transcriptionally distinct from TCM

(A) Clustering analysis of combined scRNA-seq datasets. TFH-like clusters in blue (1, 4), TCM-like in green (2) and Th1-like in red (3). (B) Dendrogram showing hierarchical

clustering. Single cells colored by cluster on x axis with tree height on y axis.

(C) Log-normalized average expression of published gene sets defining subsets.

(D) Selected genes differing between two Th1-like clusters.

(E) Heatmap showing top 20 genes segregating Th1-like clusters.

(F) Log-normalized average expression of dysfunction (left) (Ciucci et al., 2019) and exhaustion (right) genes (Martinez et al., 2015).

(G) Log-normalized average expression of published TRM signatures (Boddupalli et al., 2016; Mackay et al., 2016; Mackay et al., 2013).

(H) Flow cytometry analysis of total GP66-specific CD4 memory cells with (right) or without (left) TFH (Ly6CloPSGL1lo). Data represents one of *n* = 2 independent experiments.

Supplementary Figure 3 | TFH memory cells are constitutively glycolytic

(A) Heatmap showing scaled, centered, per-cluster expression of leading edge mTORC1-related genes (below) (Zeng et al., 2016) and HIF1-regulated genes (above) (Finlay et al., 2012).

(B) Log-normalized average expression of CAMP_PATHWAY (left) and BIOCARTA_CSK_PATHWAY (right) gene sets.

(C) Secondary analysis of published data from Cxcr5- and Cxcr5+ Smarta memory CD4 memory cells (Hale et al., 2013) following LCMV infection showing leading edge Rptor-regulated genes from Zeng et. al., 2016.

(D) Secondary analysis of data from d30 CD4 memory to LCMV showing heatmap of expression of published TFH signature genes (left) and empirical cumulative distribution of Rptor-regulated genes (right) (Ciucci et al., 2019).

(E) Flow cytometry analysis of phospho-S6 Ser240/244 (left) and MFI (right) in the different GP66-specific CD4 memory subsets Th1 (red) and TFH (blue) compared to naive CD4 T cells (grey histogram) with *n* = 2 independent experiments (each dot represents cells from individual mice, and the thin line represents the mean)

(F) Flow cytometry analysis of the indicated marker in CD44hi CD4 Th1 and TFH memory cell subsets (pregated on dump-CD4+live). Data represent at least two independent experiments with a minimum number of *n* = 3 mice per group.

(G-H) Flow cytometry histogram (left) and MFI (right) of CD98 (G) or cMyc (H) in the different GP66-specific CD4 memory subsets Th1 (red) and TFH (blue) (each dot represents cells from individual mice, and the thin line represents the mean).

(I) Quantification of basal respiration (left) and OCR profile (right) in response to oligomycin (oligo), fluoro-carbonyl cyanide phenylhydrazone (FCCP), rotenone (Rot) in sort purified Th1 (Ly6C^{hi}PSGL1^{hi}) and TFH (Ly6C^{lo}PSGL-1^{lo}) CD4 memory cells. Data are representative of *n* = 2 independent experiments.

(J) Empirical cumulative distribution of gene set HALLMARK_OXIDATIVE_PHOSPHORYLATION

(K-L) ECAR profile (K) and OCR profile (L) in response to oligomycin (oligo), fluoro-carbonyl cyanide phenylhydrazone (FCCP), rotenone (Rot) in sort purified Th1 (Ly6C^{hi}PSGL1^{hi}) and TFH (Ly6C^{lo}PSGL-1^{lo}) CD4 effector cells from day 10 post

infection pooled from 12-14 mice. Data are representative of n = 2 independent experiments.

(M) MFI of FSC-A in GP66-specific TFH memory cells treated with vehicle or 2-DG/Rapamycin. Data represents one of *n* = 2 independent experiments with the line depicting the mean and the dots individual mice.

Supplementary Figure 4 | TFH cells can survive in the absence of antigen

(A) Representative flow cytometry plot of 2-NBDG uptake (middle) in the different LCMV GP66-specific CD4 memory subsets Th1 (red), TCM (green), and TFH (blue). 2-NBDG uptake in the TFH memory compartment (right) versus expression. Data are representative of *n* = 2 independent experiments with at least 3 mice per group.

(B) Representative flow cytometry plot of 2-NBDG uptake (left) and proportion of 2-NBDG+ GP66-specific Th1 (red) or TFH (blue) memory cells (right) 412 days post infection. The line represents the mean and each dot represents cells from individual mice.

Supplementary Figure 5 | TFH memory cells give rise to multiple cell fates upon recall

(A) scRNA-seq: Rank of Cd27 among Spearman's rank correlation coefficients between Tcf7 and all other genes (left). Cd27 vs Tcf7 on imputed data (right), colored by cluster.

(B) Flow cytometry analysis (left, middle) and quantification (right) of CD27 expression in P2X7R$^{-/-}$ BM chimera mice in GP66-specific TFH (left) and Th1 memory cells (middle). Filled histograms represent wildtype cells, non-filled histograms depict P2X7R^{-}

$^{/-}$ cells.Data represent *n* = 2 independent experiments with the line depiciting the mean anddots representing cells from individual mice.

(C) Normalized average scRNA-seq expression of early memory signature (Muranski et al., 2011).

(D) Monocle2 analysis showing trajectory in pseudotime (left) and with cluster assignment (right).

(E) Monocle2 trajectory with clusters separated.

Supplementary Figure 6 | Epigenetic regulation of TFH memory T cells

(A) Venn diagramm of all called peaks in Assay for Transposase-Accessible Chromatin using sequencing (ATAC-seq) data depicting the overlap of peaks in the subsets.

(B) Number of differentially accessible regions for each genomic feature.

(C) Scatter plots of ATAC-seq promoter log2 FC and in silicio bulk RNA-seq log2 FC with blue and red arrows indicating enrichment in TFH and Th1 compartment respectively.

(D) Volcano plot of cytokine promoter region accessibility with blue and red dots indicating increased accessiblity in TFH and Th1 compartment respectively and highlighted gene tracks.

(E) Enriched motifs in Th1 memory cells found by HOMER.

(F) Heatmap depicting top transcriptional network regulators (regulons) on scRNA-seq data found by pySCENIC (Single-Cell rEgulatory Network Inference and Clustering) algorithm.

(G) GSEA analysis of the GO_RESPONSE_TO_CAMP pathway with blue and red arrows indicating enrichment in TFH and Th1 respectively.

(H) Heatmap of hierarchically clustered promoter regions with logFC > 1 in at least one comparison and FDR < 0.05.

Supplementary Figure 7 | ICOS signaling integrates TFH memory cell stemness and metabolism and contributes to late phase humoral immune responses

(A) Flow cytometry analysis (left) and MFI of TCF1 expression in GP66-specific TFH memory cells comparing PBS (solid line) and anti-ICOSL treated mice (dashed line with filled histogram). Data is representative of *n* = 2 independent experiments. The thin line represents the mean and each dot represents cells from an individual mouse.

(B) MFI of FSC-A in GP66-specific TFH memory cells comparing PBS vs anti-ICOSL treated mice. Data is representative of *n* = 2 independent experiments. The thin line represents the mean and each dot represents cells from an individual mouse.

(C) Exponential decay model showing IgG reduction after 12 days of anti-ICOSL treatment at various starting splenic contributions and assuming 100% abrogation of splenic contribution.

(D) Cell numbers of IgD, IgM or swIg NP-specific memory B cells comparing PBS and anti-ICOSL treated mice. Data summarize *n* = 2 independent experiments with dots representing individual mice and the line representing the mean.

(E) Flow cytometry analysis of NP-specific B cells. Data is representative of *n* = 2 independent experiments.

Figure 1: TFH memory cells are long-lived but susceptible to NAD induced cell death during isolation

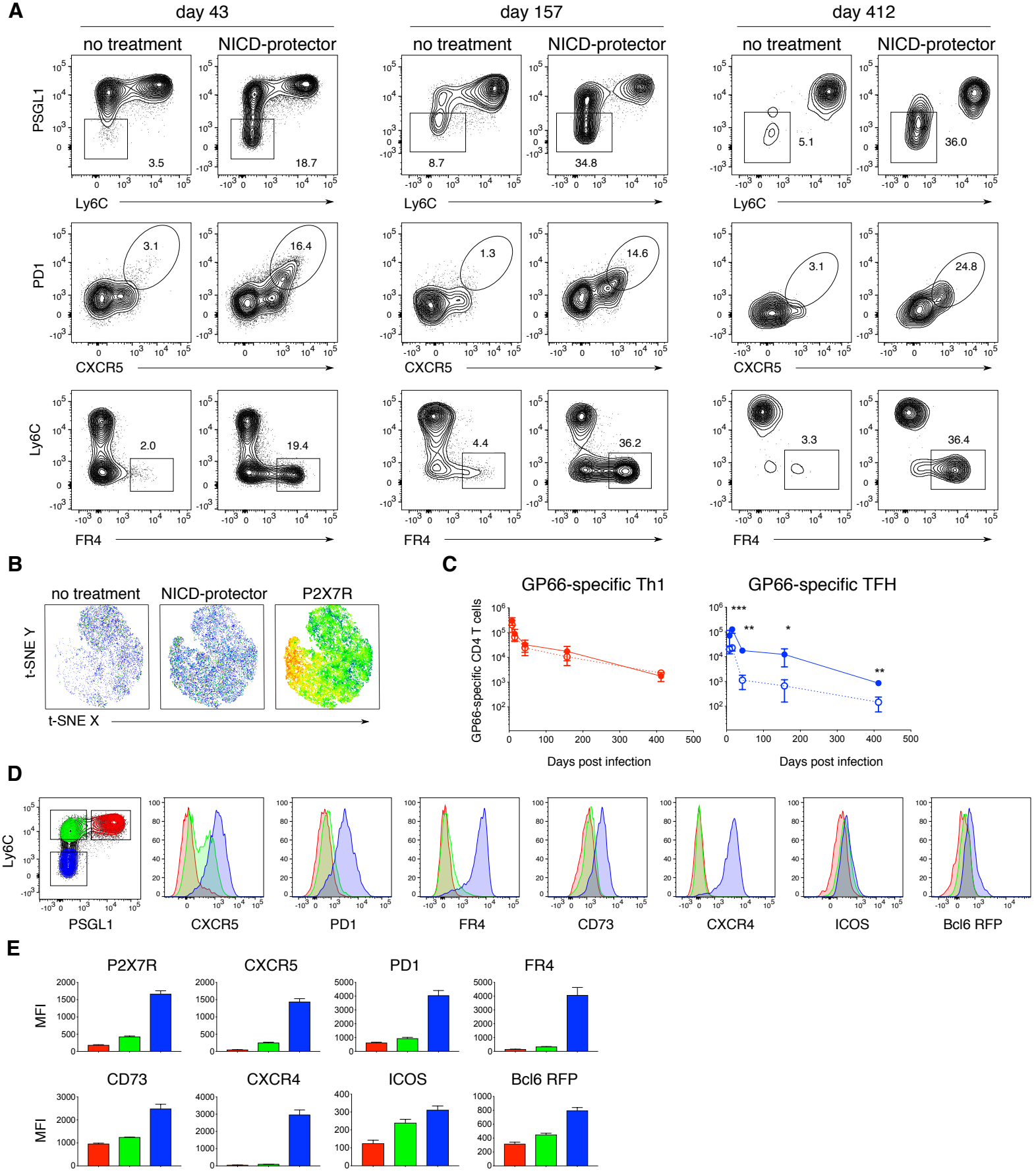

(A) Flow cytometry analysis of GP66-specific CD4 T cells isolated from the spleen at the indicated time points post infection, with or without NICD-protector using different gating strategies to identify TFH memory cells ($Ly6C^{lo}PSGL1^{lo}$ or $CXCR5^{hi}PD1^{hi}$ or $FR4^{hi}Ly6C^{lo}$).

(B) tSNE plots of the GP66-specific CD4 memory compartment with (middle, right) or without NICD-protector (left) and overlaid P2X7R expression (right).

(C) Quantification of GP66-specific Th1 (red, $Ly6C^{hi}PSGL1^{hi}$) or TFH memory cells (blue, $Ly6C^{lo}PSGL1^{lo}$) numbers over time with (solid line) or without (dashed line) NICD-protector gated as in Figure 1D. Thin lines represent the mean + s.d. (n = 3-4 mice per group).

(D-E), Representative flow cytometry plots (D) and mean fluorescence intensity (MFI) (E) of the indicated marker in GP66-specific CD4 memory cell subsets Th1 (red), TCM (green), and TFH (blue) > 40 days post infection. Data represent at least n = 2 independent experiments with a minimum number of 3 mice per group.

Figure 2: TFH memory cells are transcriptionally distinct from TCM

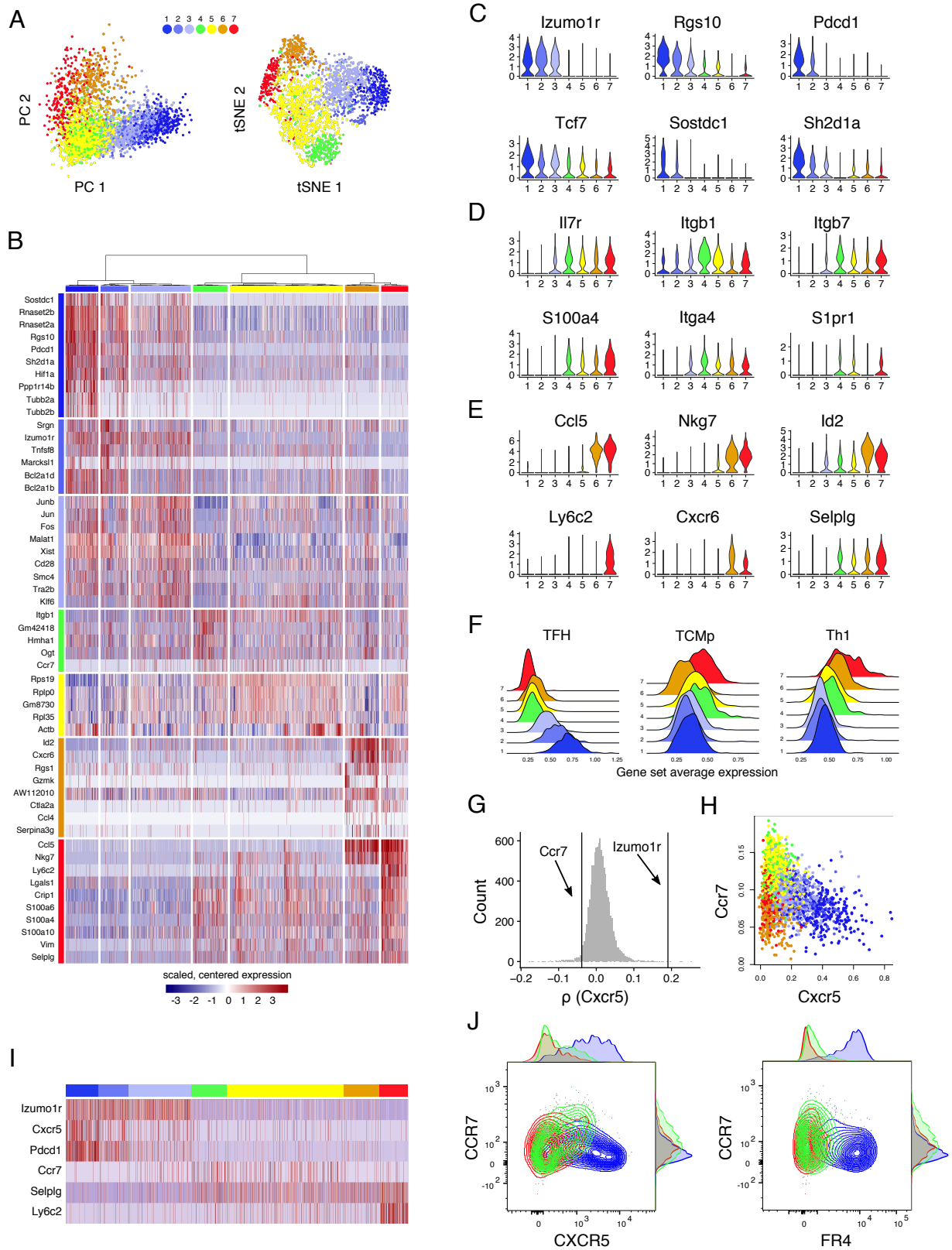

(A) Unsupervised hierarchical clustering using Ward's method: PCA and tSNE dimension reductions.
(B) Heatmap showing scaled, centered single cell expression data of top 10 cluster-defining genes by cluster.
(C-E) Log-normalized expression of genes typical for TFH (C), TCM (D) and Th1 (E) populations.
(F) Log-normalized average expression of published CD4 signatures obtained by analysis of d7 effectors: TFH, TCM precursors, and Th1.
(G) scRNA-seq: Rank of Ccr7 and Izumo1r (encoding FR4) among Spearman's rank correlation coefficients between Cxcr5 and all other genes.
(H) scRNA-seq: Cxcr5 vs Ccr7 on imputed data, colored by cluster. Dropout imputed using Seurat::AddImputedScore unless otherwise noted.
(I) Scaled, centered single cell expression of Izumo1r in comparison to other common gating markers. Unless otherwise noted, scRNA-seq data are shown from the run with NICD-protector to ensure consistency with other experiments.
(J) Flow cytometric analysis of CCR7, CXCR5 and FR4 on GP-66 specific CD4 memory cells >50 days post infection gated as in Figure 1D.

Figure 3: TFH memory cells are constitutively glycolytic

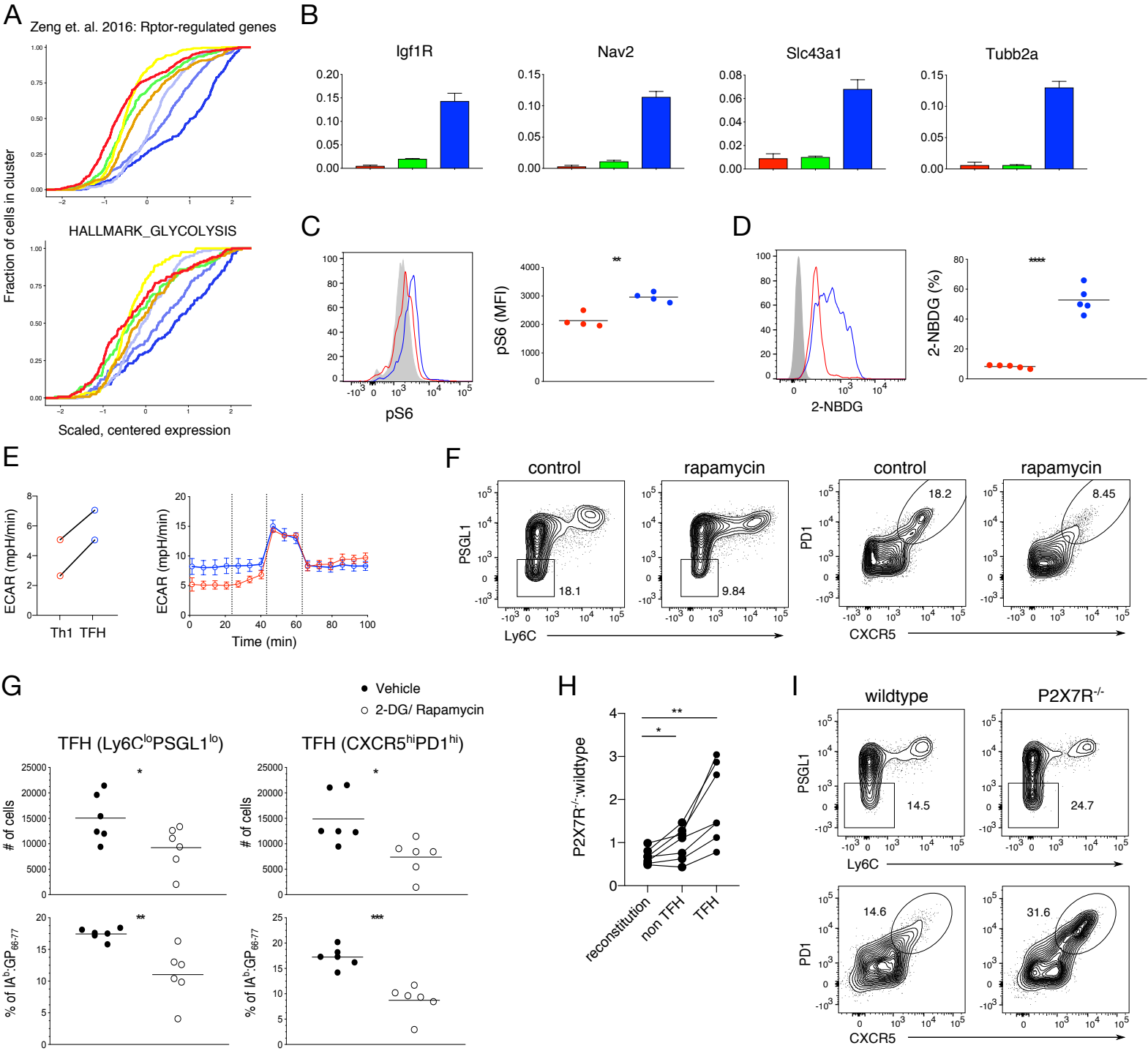

(A) Empirical cumulative distribution of scaled, centered mRNA expression by cluster of Rptor-regulated genes (above) (Chi Zeng) and the gene set HALLMARK_GLYCOLYSIS (below).

(B) quantitative PCR of indicated genes (arbitrary units (AU) relative to Rpl13a) in sort-purified GP66-specific Th1 (red, Ly6C^{hi}PSGL1^{hi}), TCM (green, Ly6C^{lo}PSGL1^{hi}) and TFH (blue, Ly6C^{lo}PSGL-1^{lo}) CD4 memory cells. Data is representative of *n* = 2 independent experiments depicting the mean +s.d. of three technical replicates.

(C-D) Representative flow cytometry histograms and MFI from one experiment of intracellular phospho-S6 Ser240/244 on CD44^{+} CD4 Th1 (red) or TFH (blue) memory cells compared to naive CD4 T cells (grey histogram) (C) and 2-NBDG uptake (D) on GP66-specific CD4 memory cells >30 days post infection compared to FMO control (grey histogram) with *n* = 2 independent experiments (each dot represents cells from individual mice, and the thin line represents the mean).

(E) Quantification of basal ECAR (left) and ECAR profile (right) in response to oligomycin (oligo), fluoro-carbonyl cyanide phenylhydrazone (FCCP), rotenone (Rot) in sort purified Th1 (red, Ly6C^{hi}PSGL1^{hi}) and TFH (blue, Ly6C^{lo}PSGL-1^{lo}) CD4 memory cells pooled from 20-30 mice. Data are representative of n = 2 independent experiments.

(F-G) Representative plots (F) of flow cytometric analysis of GP66-specific CD4 memory cells treated with vehicle or 2-DG/ Rapamycin of *n* = 2 independent experiments and cell numbers and proportions of GP66-specific TFH memory cells using either Ly6C^{lo}PSGL1^{lo} or CXCR5^{hi}PD1^{hi} as gating strategy (G). Each dot represents cells from individual mice, and the thin line represents the mean.

(H) P2X7R$^{-/-}$ to wildtype ratio of GP66-specific CD4 memory cells in BM chimera mice >60 days post infection compared to ratio of total CD4 compartment after reconstitution. Data represent *n* = 2 independent experiments with each dot and connecting line represents one individual mouse.

(I) Flow cytometric analysis of GP66-specific CD4 memory cells in P2X7R$^{-/-}$ or wildtype compartment using either Ly6C^{lo}PSGL1^{lo} or CXCR5^{hi}PD1^{hi} as gating strategy to identify TFH memory cells >60 days post infection.

Figure 4: TFH memory cells can survive in the absence of antigen

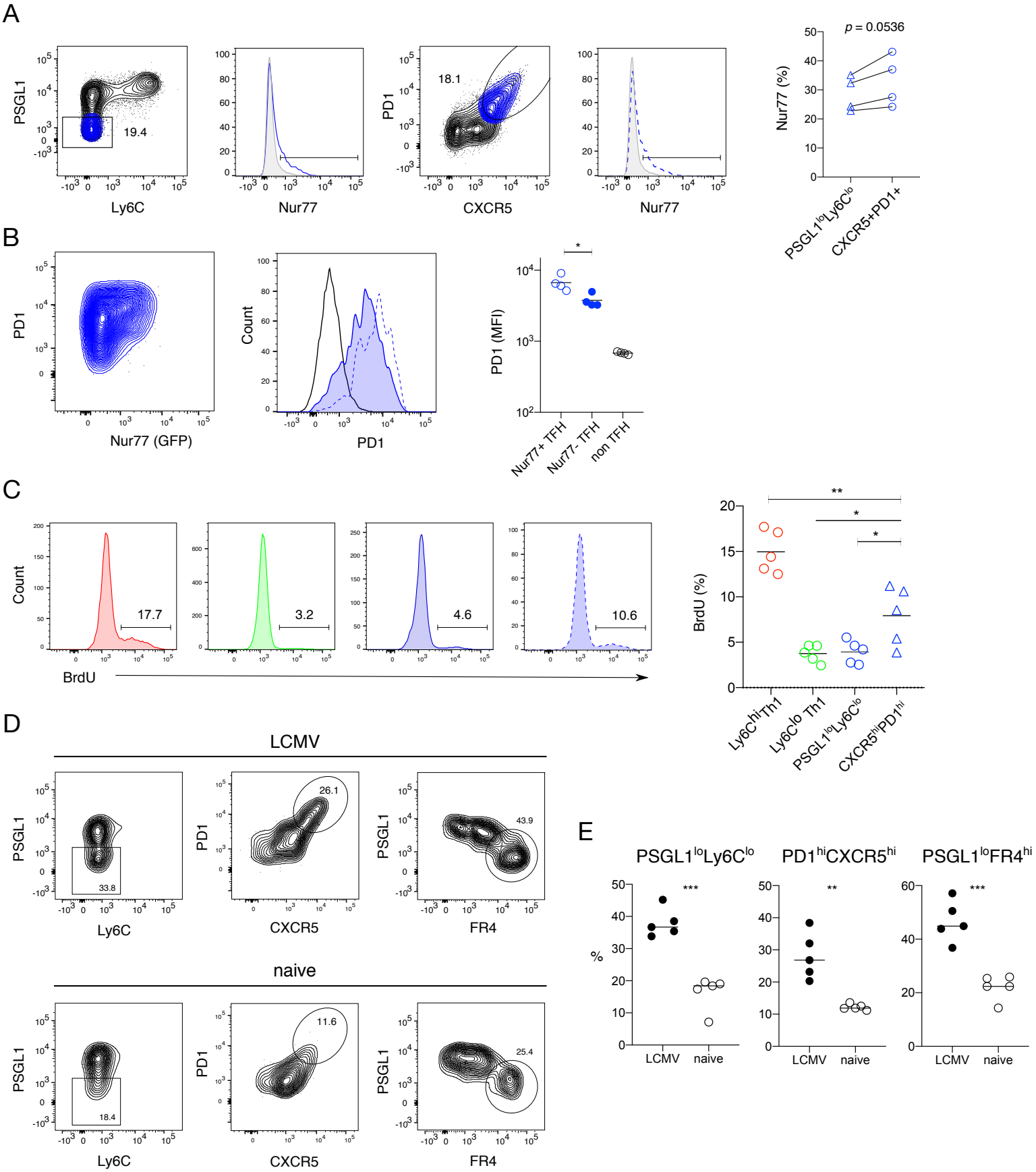

(A) Flow cytometry analysis of Nur77 expression by GP66-specific TFH memory cells for the indicated gating strategies.
(B) Representative flow cytometry plots (left panels) and MFI (right panel) depicting PD1 expression on Nur77+ (dotted blue line) and Nur77- (tinted blue line) TFH cells, gated as depicted in panel (A).
(C) Flow cytometry plots (left) and quantification (right) of BrdU incorporation by GP66-specific CD4 memory subsets.
(D-E) Total GP66-specific CD4 T cells were isolated at day 10 after LCMV infection and transferred into congenic infection matched (LCMV) or naive mice. Donor cell phenotype was analyzed at day 30 after infection. Representative flow cytometry plots (D) and quantification (E) with gating for PSGL1^{lo}Ly6C^{lo} (left), PD1^{hi}CXCR5^{hi} (middle) and PSGL1^{lo}FR4^{hi} (right). Data represent n = 2 independent experiments and each dot represents cells from individual mice, and the line marks the mean.

Figure 5: TFH memory cells give rise to multiple cell fates upon recall

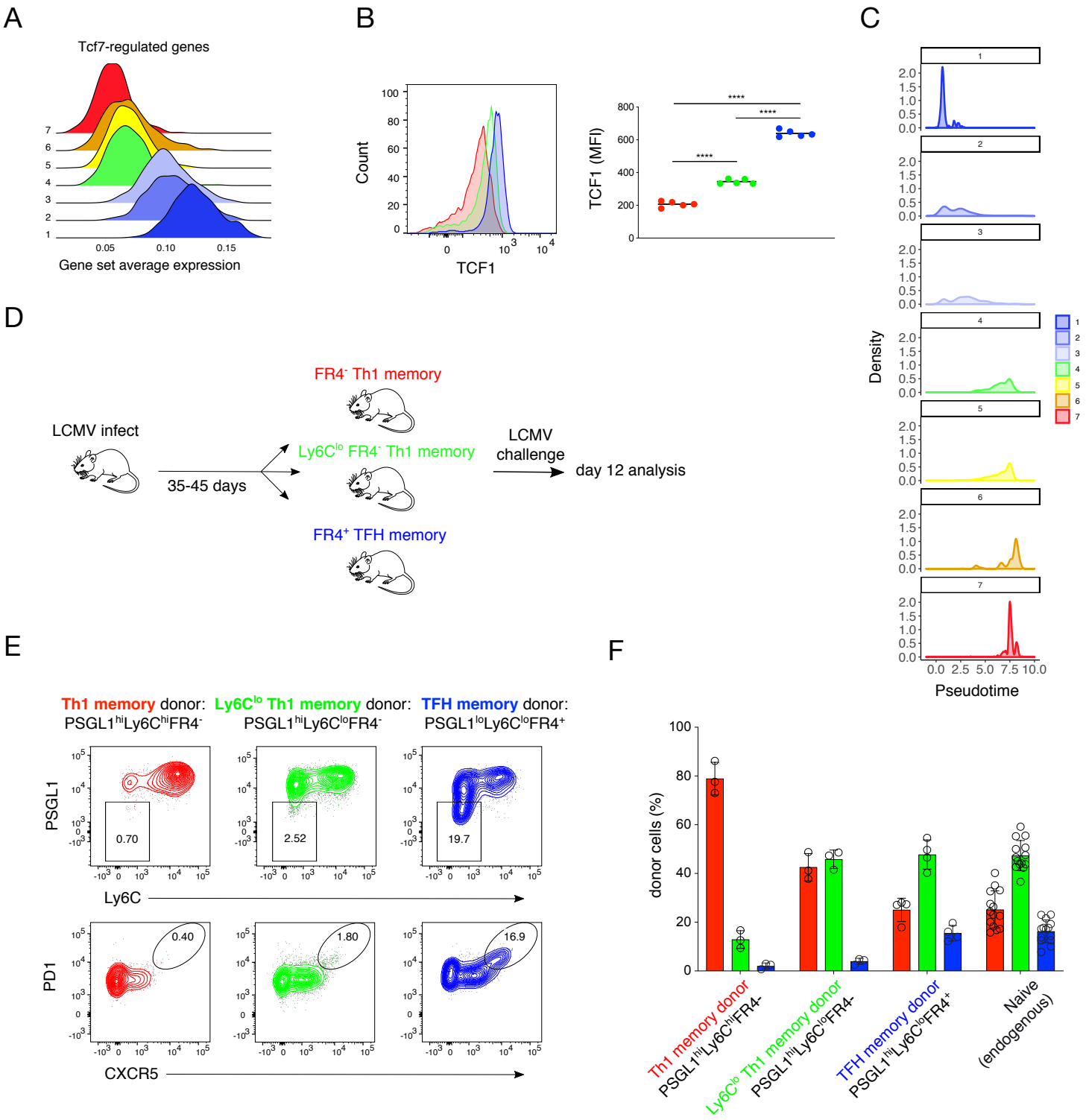

(A) Log-normalized average expression of genes tracking with Tcf7 (Utzschneider et. al. 2016).
(B) Flow cytometry analysis of TCF1(left) and MFI (right) in Th1 (red), Ly6C^{lo} Th1 (green) and TFH (blue) GP66-specific memory cells. Data represents n = 2 independent experiments with 5 mice each.
(C) Density of cells in pseudotime, Monocle2 analysis.
(D) GP66-specific Ly6C^{hi} Th1, Ly6C^{lo} Th1 or TFH CD4 memory T cells were sorted at day 35-45 after LCMV infection and transferred into congenic naive mice. The recipient mice were challenged with LCMV the following day. Donor cellphenotype was analyzed at day 12 after infection.
(E) Representative plots of flow cytometric analysis of Ly6C^{hi} Th1 (red), Ly6C^{lo} Th1 (green) or TFH (blue) donor cell phenotype.
(F) Quantification of Ly6C^{hi} Th1 effectors (red), Ly6C^{lo} Th1(green) and TFH (blue) effectors from Ly6C^{hi} Th1, Ly6C^{lo} Th1 or TFH donors compared to endogenous response.

Figure 6: Epigenetic regulation of TFH memory T cells

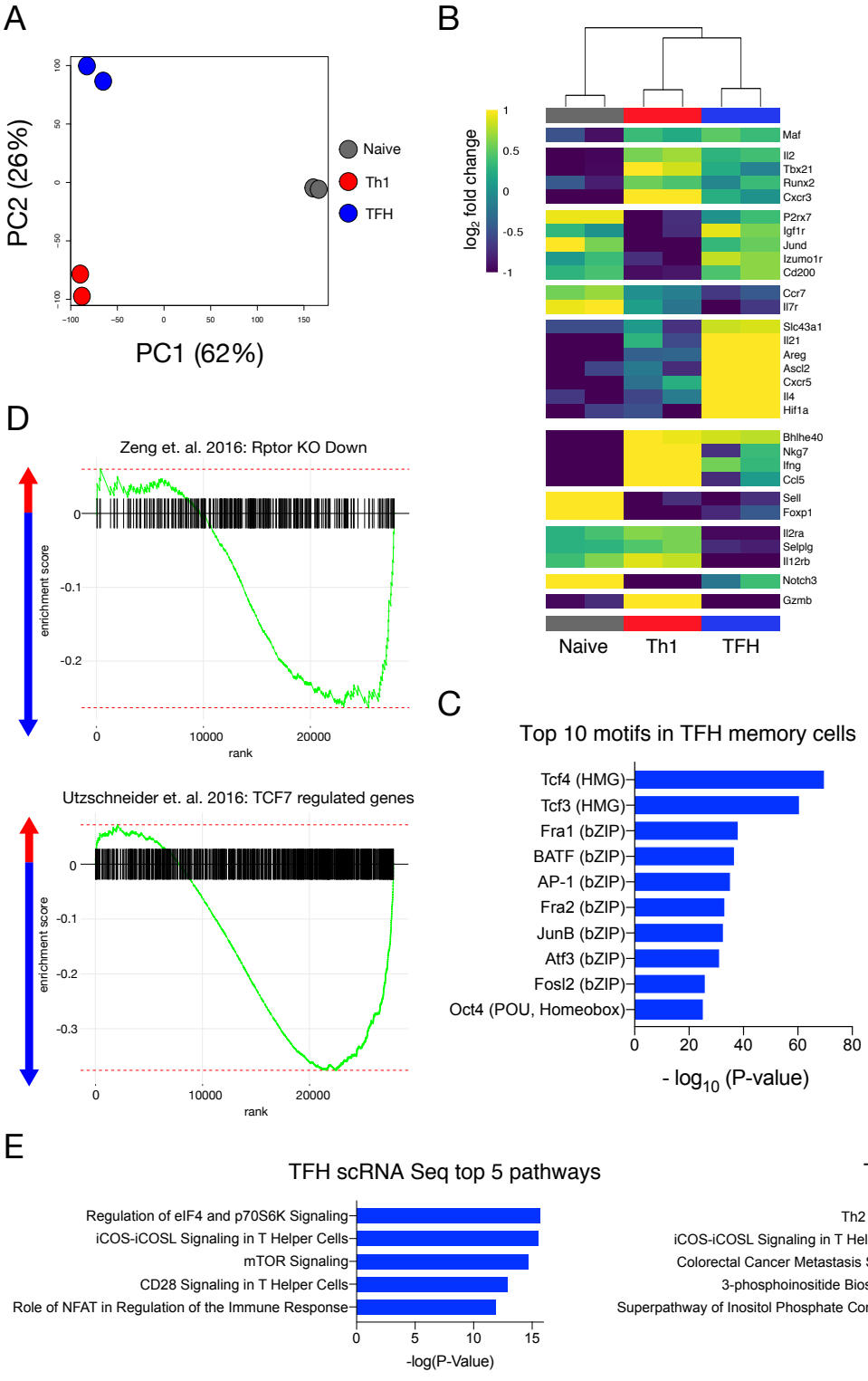

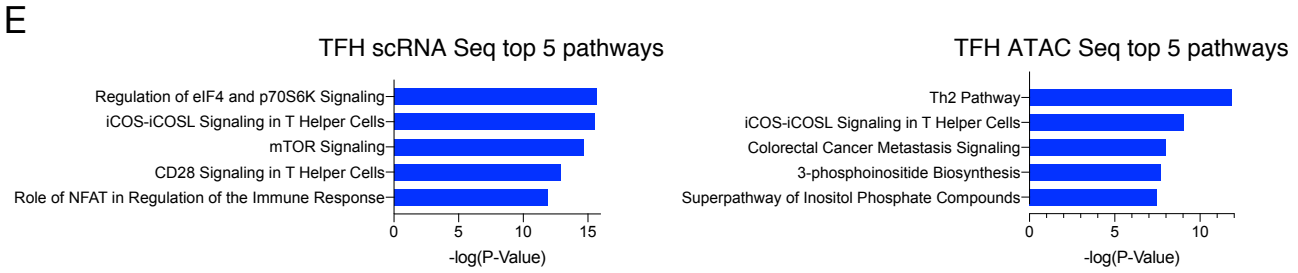

(A) PCA of Assay for Transposase-Accessible Chromatin using sequencing (ATAC-seq) data on all peaks.
(B) Heatmap of hierarchically clustered promoter regions of highlighted genes.
(C) Enriched motifs in TFH memory cells found by HOMER.
(D) GSEA analysis of Rptor (above) and Tcf7 (below) regulated genes with negative enrichment score indicating enrichment in TFH memory and positive score indicating enrichment in Th1 memory.
(E) Top 5 pathways enriched in TFH memory cells determined by Ingenuity Pathway Analysis in: combined scRNA-seq data (with and without NICD-protector) comparing TFH cluster to Th1 cluster from 3-cluster version (left) and ATAC-seq peaks mapped to nearest TSS within TAD (right).

Figure 7: ICOS signaling integrates TFH memory cell stemness and metabolism and contributes to late phase humoral immune responses

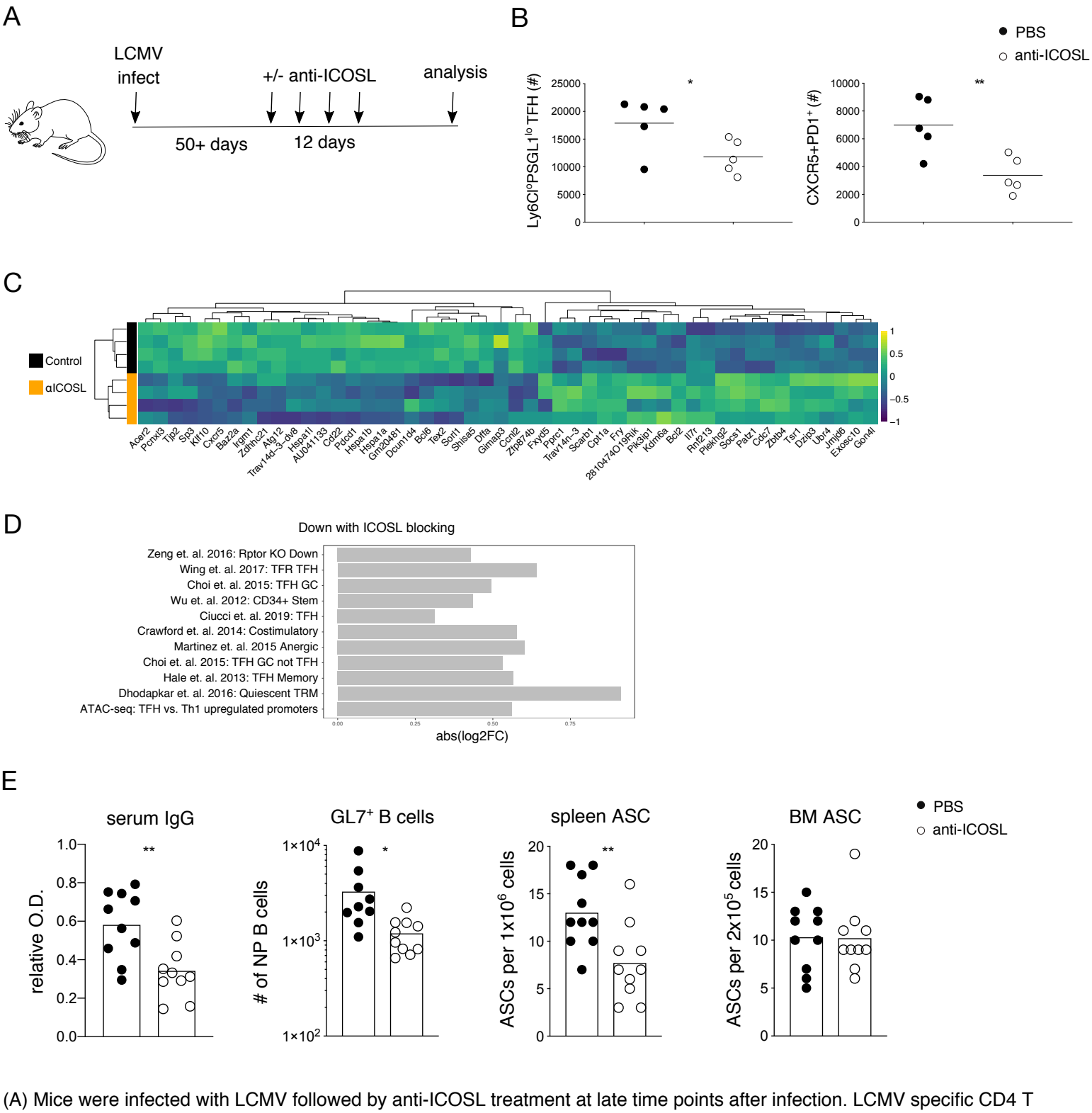

(A) Mice were infected with LCMV followed by anti-ICOSL treatment at late time points after infection. LCMV specific CD4 T cells and B cells were analyzed after 12 days of treatment.
(B) Cell numbers of GP66-specific TFH memory cells in treated mice using either Ly6C^{lo}PSGL1^{lo} or CXCR5^{hi}PD1^{hi} as gating strategy. Data represents one of $n = 2$ independent experiments.
(C) Scaled, centered expression of 20 most significant differentially expressed transcripts in TFH memory cells between control and anti-ICOSL treated mice.
(D) Most significantly downregulated gene signatures with anti-ICOSL blocking (FDR < 0.2).
(E) NP-specific IgG serum titer (far left), numbers of NP-specific GL7^{+} B cells (left) and NP-specific antibody secreting cells from the spleen (right) and bone marrow (far right). Data summarize $n = 2$ independent experiments with dots representing individual mice and bars indicating the mean.

Supplementary Figure 1: TFH memory cells are long-lived but susceptible to NAD induced cell death during isolation

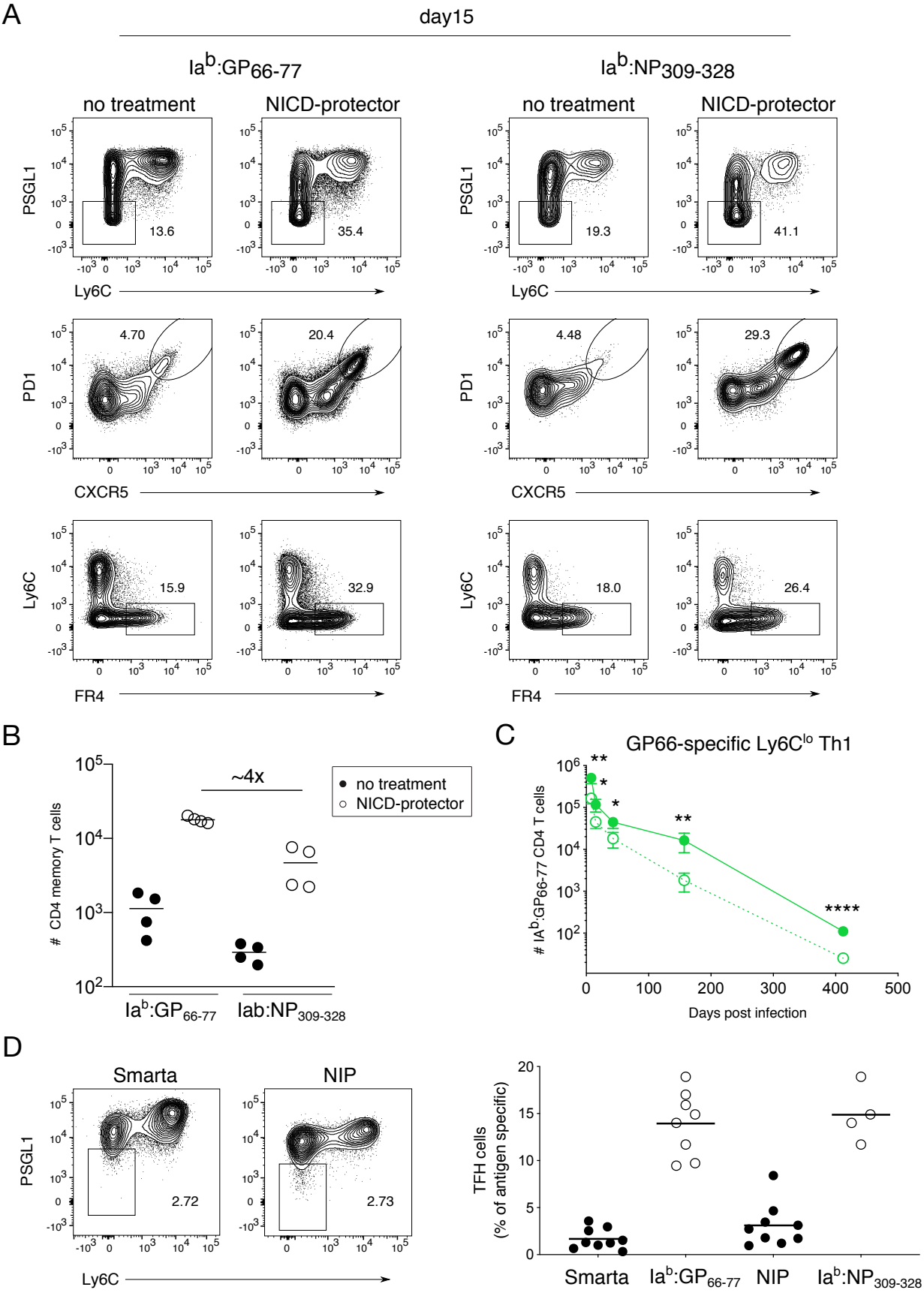

(A) Flow cytometry analysis of GP66-specific CD4 T cells isolated from the spleen at day 15 post infection, with or without NICD-protector comparing the GP66 epitope to the NP epitope. Different gating strategies were used to identify TFH memory cells (PSGL1^{lo}Ly6C^{lo} or PD1^{hi}CXCR5^{hi} or Ly6C^{lo}FR4^{hi}).
(B) Comparison of total epitope-specific CD4 memory cell numbers in control and NICD-protector treated mice >30 days post infection (each dot represents cells from individual mice, and the thin line represents the mean).
(C) Quantification of GP66-specific Ly6C^{lo} Th1 memory cells (green, Ly6C^{lo}PSGL1^{hi} gated as in Fig 1D over time with (solid line) or without (dashed line) NICD-protector. Thin lines represent the mean + s.d. (n = 3-4 mice per group).
(D) Representative flow cytometry plots (left) and proportions of TFH memory cells (right) in TCR-transgenic Smarta and NIP memory cells compared to polyclonal GP66-specific and NP-specific CD4 memory compartment >30 days post infection. Data summarize n = 2 independent experiments for each group (each dot represents cells from individual mice, and the line represents the mean).

Supplementary Figure 2: TFH memory cells are transcriptionally distinct from TCM

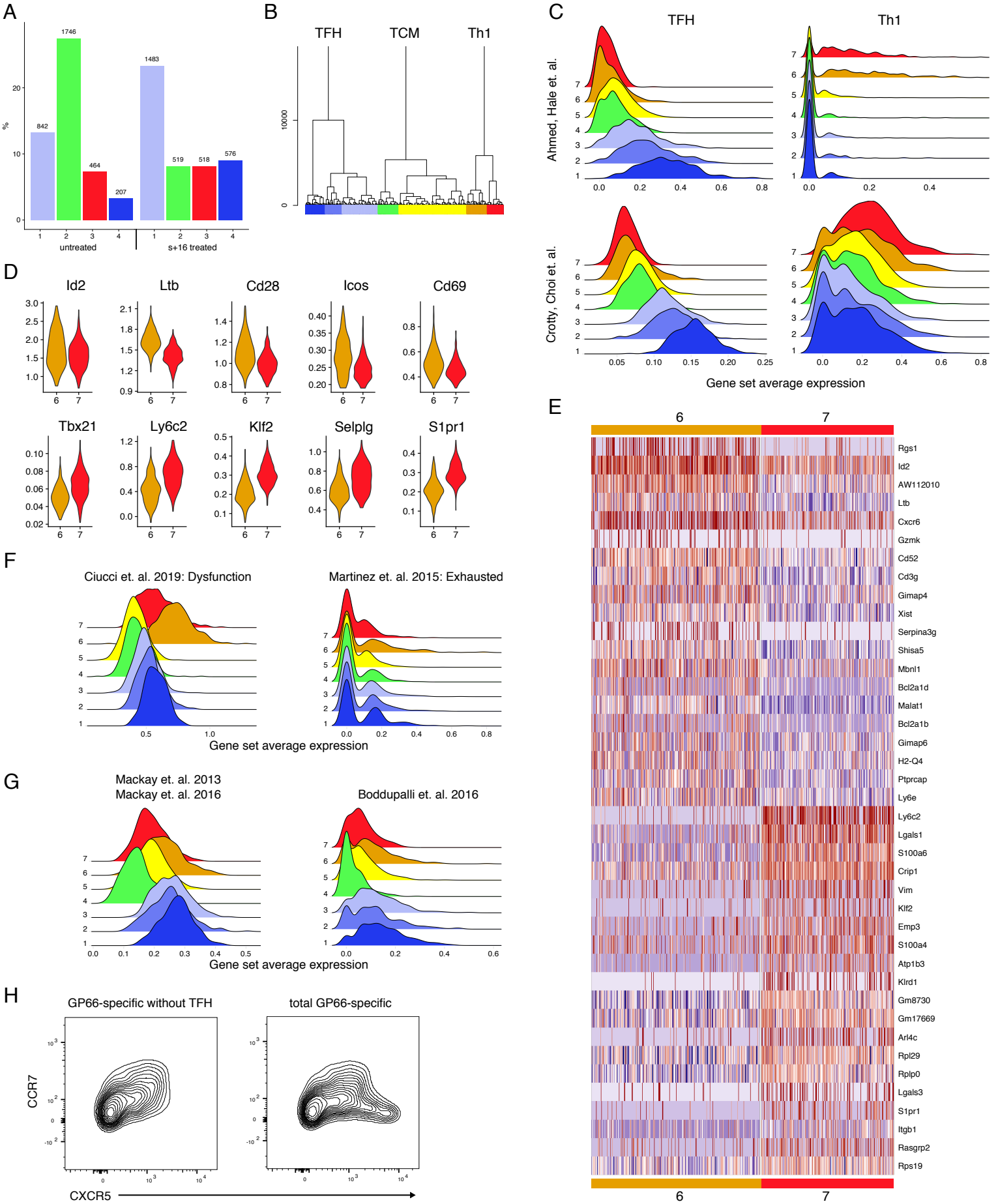

(A) Clustering analysis of combined scRNA-seq datasets. TFH-like clusters in blue (1, 4), TCM-like in green (2) and Th1-like in red (3).
(B) Dendrogram showing hierarchical clustering. Single cells colored by cluster on x axis with tree height on y axis.
(C) Log-normalized average expression of published gene sets defining subsets.
(D) Selected genes differing between two Th1-like clusters.
(E) Heatmap showing top 20 genes segregating Th1-like clusters.
(F) Log-normalized average expression of dysfunction (left) and exhaustion (right) genes.
(G) Log-normalized average expression of published TRM signatures.
(H) Flow cytometry analysis of total GP66-specific CD4 memory cells with (right) or without (left) TFH (Ly6C^{lo}PSGL1^{lo}). Data represents one of $n = 2$ independent experiments.

Supplementary Figure 3: TFH memory cells are constitutively glycolytic

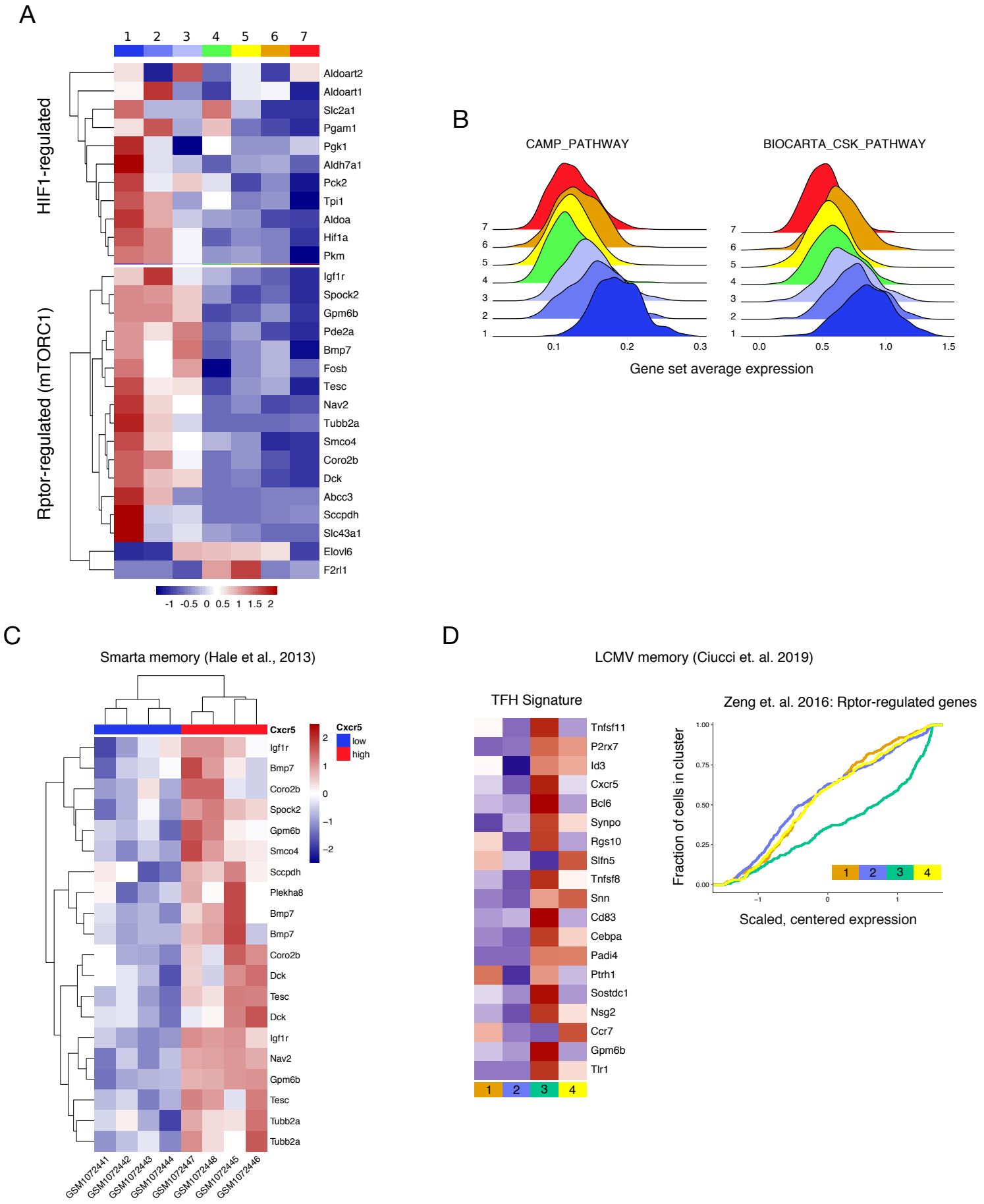

(A) Heatmap showing scaled, centered, per-cluster expression of leading edge mTORC1-related genes (below) (Zeng et. al. 2016) and HIF1-regulated genes (above) (Finlay et. al. 2012).
(B) Log-normalized average expression of CAMP_PATHWAY (left) and BIOCARTA_CSK_PATHWAY (right) gene sets.
(C) Secondary analysis of published data from Cxcr5- and Cxcr5+ Smarta memory CD4 memory cells following LCMV infection showing leading edge Rptor-regulated genes from Zeng et. al. 2016.
(D) Secondary analysis of data from d30 CD4 memory to LCMV showing heatmap of expression of published TFH signature genes (left) and empirical cumulative distribution of Rptor-regulated genes (right).

Supplementary Figure 3: TFH memory cells are constitutively glycolytic

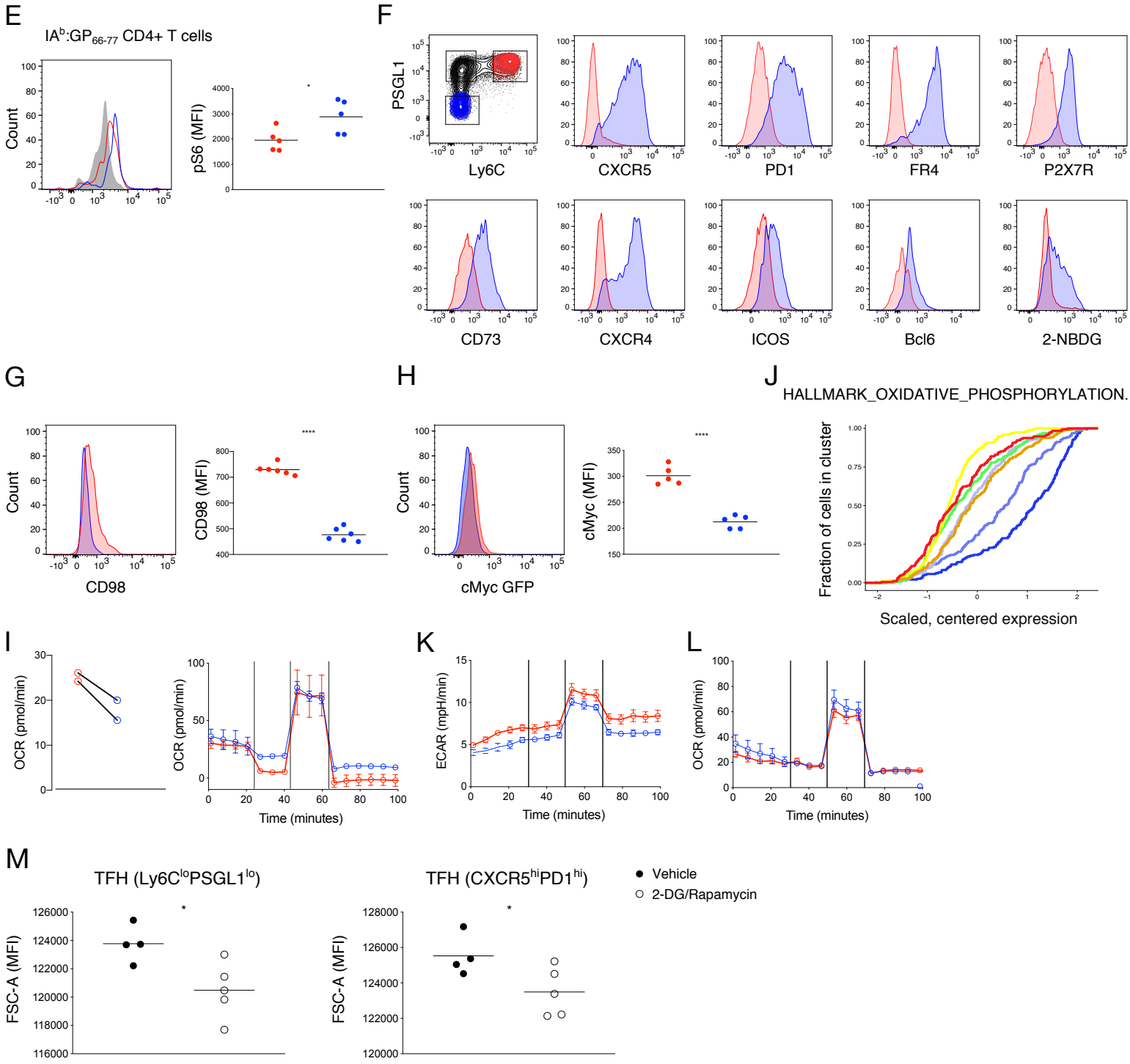

(E) Flow cytometry analysis of phospho-S6 Ser240/244 (left) and MFI (right) in the different GP66-specific CD4 memory subsets Th1 (red) and TFH (blue) compared to naive CD4 T cells (grey histogram) with $n = 2$ independent experiments (each dot represents cells from individual mice, and the thin line represents the mean)

(F) Flow cytometry analysis of the indicated marker in CD44^{hi} CD4 Th1 and TFH memory cell subsets (pregated on dump$^-$CD4$^+$live). Data represent at least two independent experiments with a minimum number of $n = 3$ mice per group.

(G-H) Flow cytometry histogram (left) and MFI (right) of CD98 (G) or cMyc (H) in the different GP66-specific CD4 memory subsets Th1 (red) and TFH (blue) (each dot represents cells from individual mice, and the thin line represents the mean).

(I) Quantification of basal respiration (left) and OCR profile (right) in response to oligomycin (oligo), fluoro-carbonyl cyanide phenylhydrazone (FCCP), rotenone (Rot) in sort purified Th1 (Ly6C^{hi}PSGL1^{hi}) and TFH (Ly6C^{lo}PSGL-1^{lo}) CD4 memory cells. Data are representative of $n = 2$ independent experiments.

(J) Empirical cumulative distribution of gene set HALLMARK_OXIDATIVE_PHOSPHORYLATION

(K-L) ECAR profile (K) and OCR profile (L) in response to oligomycin (oligo), fluoro-carbonyl cyanide phenylhydrazone (FCCP), rotenone (Rot) in sort purified Th1 (Ly6C^{hi}PSGL1^{hi}) and TFH (Ly6C^{lo}PSGL-1^{lo}) CD4 effector cells from day 10 post infection pooled from 12-14 mice. Data are representative of $n = 2$ independent experiments.

(M) MFI of FSC-A in GP66-specific TFH memory cells treated with vehicle or 2-DG/Rapamycin. Data represents one of $n = 2$ independent experiments with the line depicting the mean and the dots individual mice.

Supplementary Figure 4: TFH memory cells can survive in the absence of antigen

A

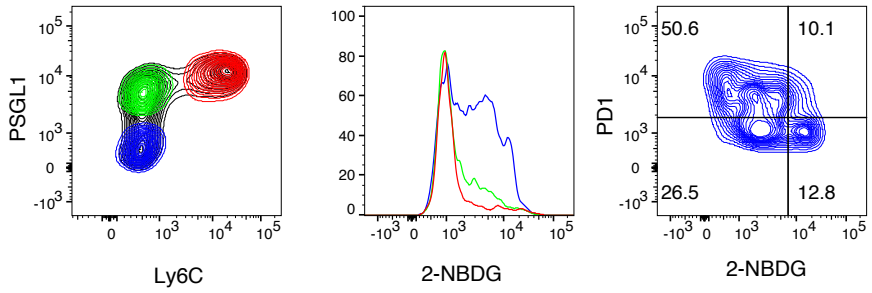

B

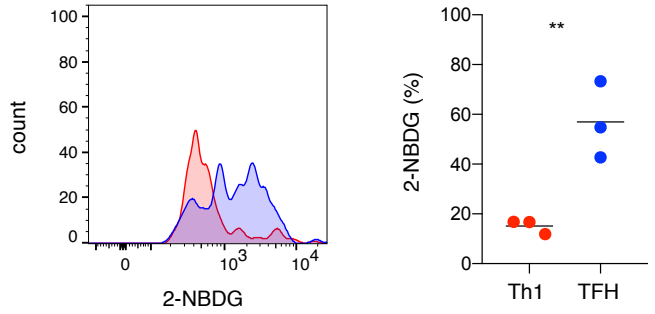

(A) Representative flow cytometry plot of 2-NBDG uptake (middle) in the different LCMV GP66-specific CD4 memory subsets Th1 (red), TCM (green), and TFH (blue). 2-NBDG uptake in the TFH memory compartment (right) versus PD-1 expression. Data are representative of $n = 2$ independent experiments with at least 3 mice per group.
(B) Representative flow cytometry plot of 2-NBDG uptake (left) and proportion of 2-NBDG+ GP66-specific Th1 (red) or TFH (blue) memory cells (right) 412 days post infection. The line represents the mean and each dot represents cells from individual mice.

Supplementary Figure 5: TFH memory cells give rise to multiple cell fates upon recall

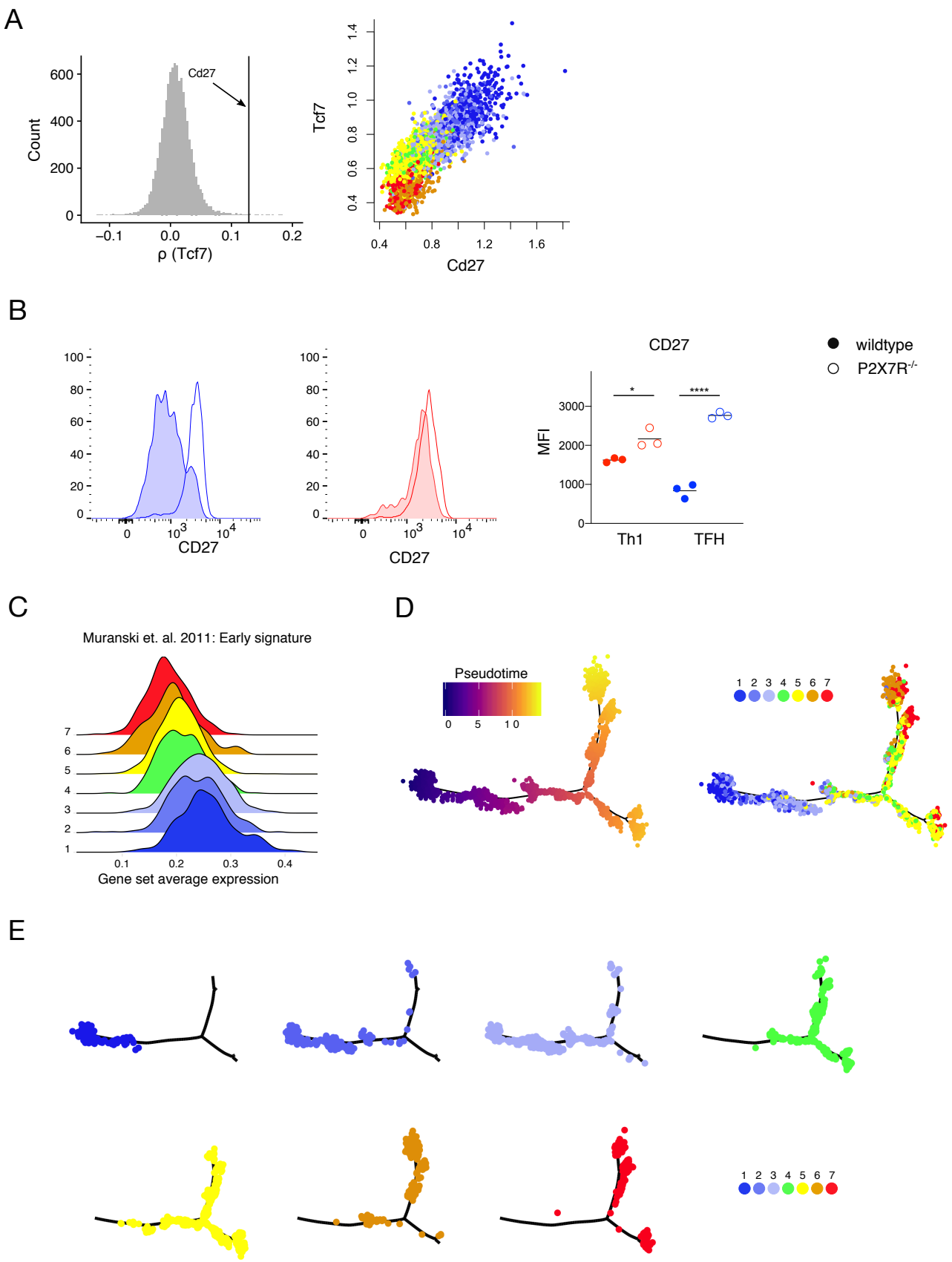

(A) scRNA-seq: Rank of Cd27 among Spearman's rank correlation coefficients between Tcf7 and all other genes (left). Cd27 vs Tcf7 on imputed data (right), colored by cluster.
(B) Flow cytometry analysis (left, middle) and quantification (right) of CD27 expression in P2X7R$^{-/-}$ BM chimera mice in GP66-specific TFH (left) and Th1 memory cells (middle). Filled histograms represent wildtype cells, non-filled histograms depict P2X7R$^{-/-}$ cells.
Data represent n = 2 independent experiments with the line depiciting the mean anddots representing cells from individual mice.
(C) Normalized average scRNA-seq expression of early memory signature.
(D) Monocle2 analysis showing trajectory in pseudotime (left) and with cluster assignment (right).
(E) Monocle2 trajectory with clusters separated.

Supplementary Figure 6: Epigenetic regulation of TFH memory T cells

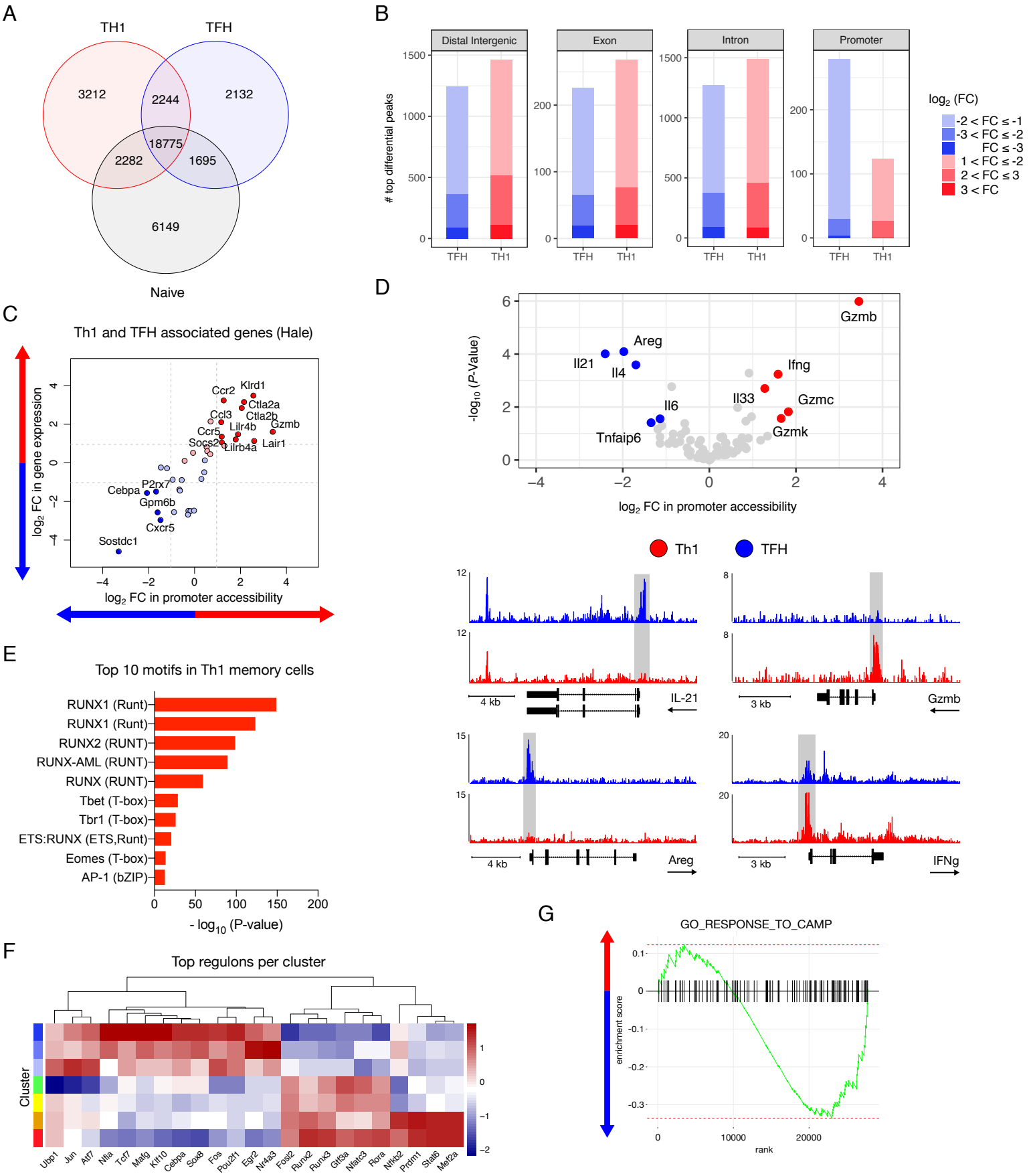

(A) Venn diagramm of all called peaks in Assay for Transposase-Accessible Chromatin using sequencing (ATAC-seq) data depicting the overlap of peaks in the subsets.
(B) Number of differentially accessible regions for each genomic feature.
(C) Scatter plots of ATAC-seq promoter $\log_2$ FC and in silicio bulk RNA-seq $\log_2$ FC with blue and red arrows indicating enrichment in TFH and Th1 compartment respectively.
(D) Volcano plot of cytokine promoter region accessibility with blue and red dots indicating increased accessiblity in TFH and Th1 compartment respectively and highlighted gene tracks.
(E) Enriched motifs in Th1 memory cells found by HOMER.
(F) Heatmap depicting top transcriptional network regulators (regulons) on scRNA-seq data found by pySCENIC (Single-Cell rEgulatory Network Inference and Clustering) algorithm.
(G) GSEA analysis of the GO_RESPONSE_TO_CAMP pathway with blue and red arrows indicating enrichment in TFH and Th1 respectively.

Supplementary Figure 6: Epigenetic regulation of TFH memory T cells

H

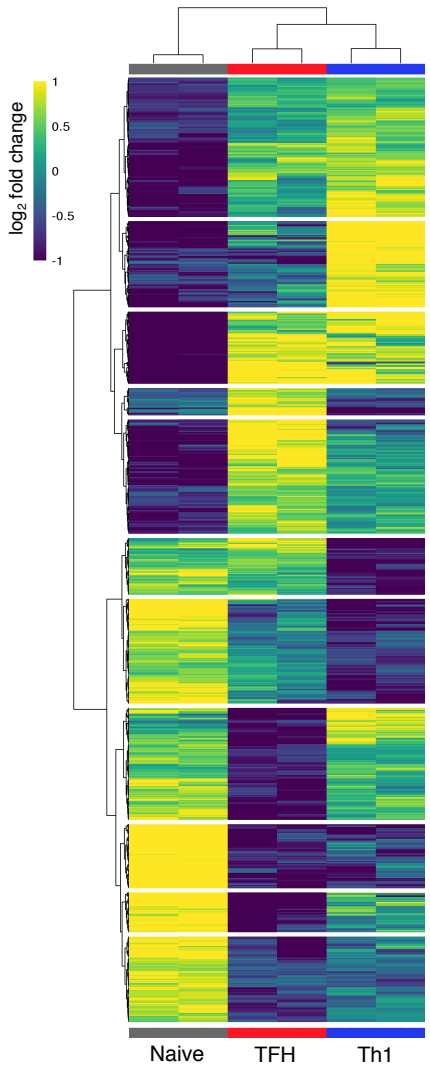

(H) Heatmap of hierarchically clustered promoter regions with logFC > 1 in at least one comparison and FDR < 0.05

Supplementary Figure 7: ICOS signaling integrates TFH memory cell stemness and metabolism and contributes to late phase humoral immune responses

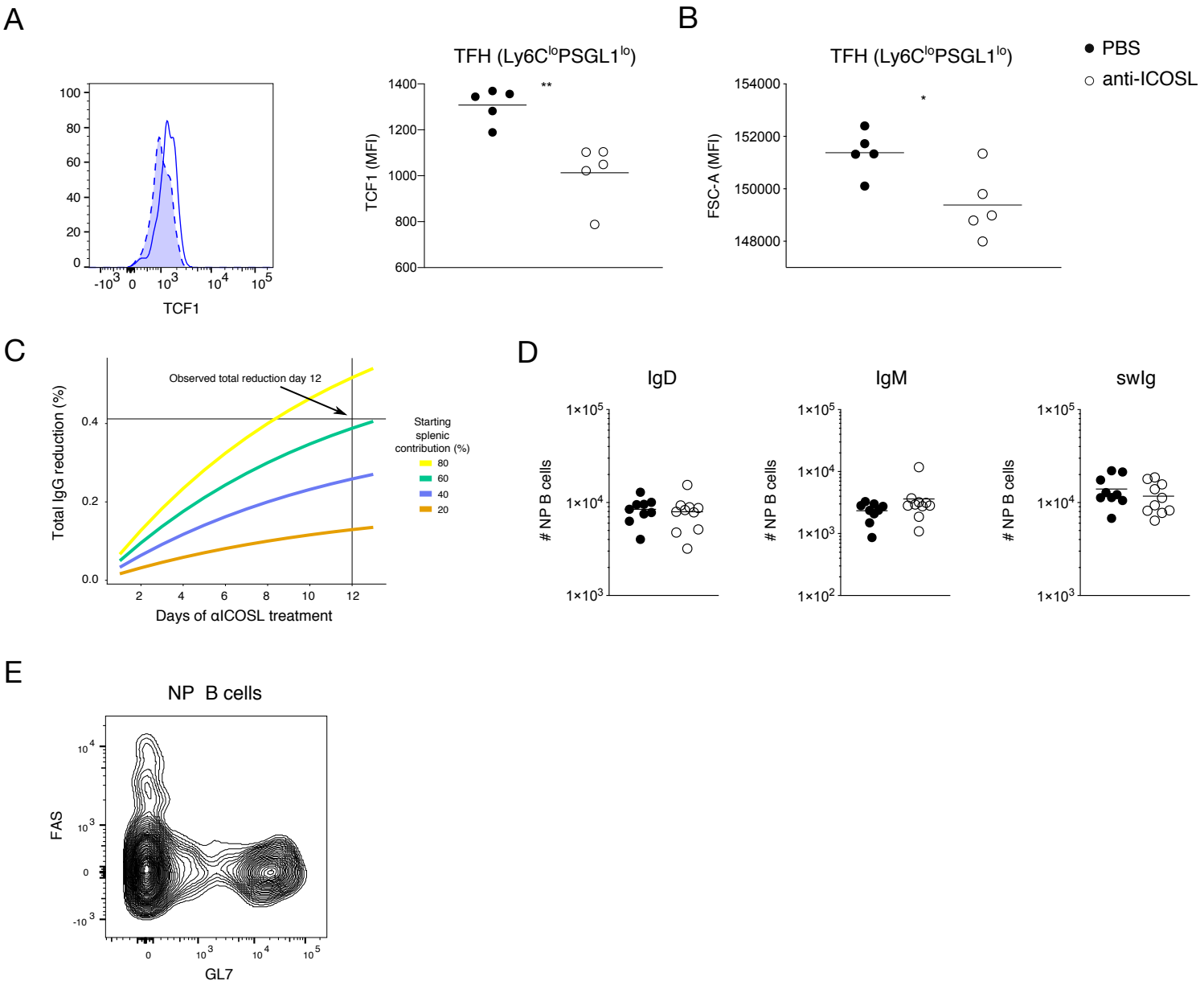

(A) Flow cytometry analysis (left) and MFI of TCF1 expression in GP66-specific TFH memory cells comparing PBS (solid line) and anti-ICOSL treated mice (dashed line with filled histogram). Data is representative of $n = 2$ independent experiments. The thin line represents the mean and each dot represents cells from an individual mouse.
(B) MFI of FSC-A in GP66-specific TFH memory cells comparing PBS vs anti-ICOSL treated mice. Data is representative of $n = 2$ independent experiments. The thin line represents the mean and each dot represents cells from an individual mouse.
(C) Exponential decay model showing IgG reduction after 12 days of anti-ICOSL treatment at various starting splenic contributions and assuming 100% abrogation of splenic contribution.
(D) Cell numbers of IgD, IgM or swIg NP-specific memory B cells comparing PBS and anti-ICOSL treated mice. Data summarize $n = 2$ independent experiments with dots representing individual mice and the line representing the mean.
(E) Flow cytometry analysis of NP-specific B cells. Data is representative of $n = 2$ independent experiments.